TECHNISCHE UNIVERSITÄT WIEN
Vienna | Austria

D I P L O M A R B E I T

Ceria based cathodes for CO_2 electrolysis in solid oxide cells

AUSGEFÜHRT AM INSTITUT FÜR

CHEMISCHE TECHNOLOGIEN UND ANALYTIK

DER TECHNISCHEN UNIVERSITÄT WIEN

UNTER ANLEITUNG VON

Univ.-Prof. Dipl.-Phys. Dr.rer.nat. Jürgen Fleig

Univ.Ass. Dipl.-Ing. Dr.techn. Alexander Karl Opitz

Univ.Ass. Dipl.-Ing. Dr.rer.nat Andreas Nenning

DURCH

Maximilian Humer, BSc.

Wien, 18.Jänner 2020

Sehr geehrte Leserin! Sehr geehrter Leser!

Nach Vollendung dieser Arbeit blicke ich nun wesentlich entspannter auf die vielen Stunden im Labor, des Auswertens, Besprechens und Schreibens, die dazu nötig waren, zurück.

Ich möchte mich an dieser Stelle bei jenen bedanken, die mir den Weg bis hierher ermöglicht haben und mir zur Seite gestanden sind.

Zuerst möchte ich meinen Dank an Professor Jürgen Fleig und an Alexander Opitz richten, welche mir die Möglichkeit gaben, die Diplomarbeit in dieser Abteilung zu absolvieren und mir weiterhalfen, wenn ich mir keinen Reim auf Resultate machen konnte.

Als zweites möchte ich mich bei meinem Betreuer bedanken. Wann immer Fragen auftraten, Geräte nicht funktionierten oder Besprechungen über den weiteren Arbeitsverlauf nötig waren, warst Du zur Stelle. Daher, größten Dank Andi.

Auch meinen Zimmerkollegen am Institut, Josef und Christoph, will ich hierbei Platz einräumen, da Sie in Momenten der Frustration stets für gute Laune und Abwechslung mit interessanten Gesprächen gesorgt haben.

Jetzt ist es an der Zeit meiner Familie und im Besonderen meinen Eltern zu danken, die mich stets motiviert, unterstützt und mir die Möglichkeit gegeben haben überhaupt zu studieren. Da ich ohne Euch keinesfalls so weit gekommen wäre und für alles andere, was hier zu erwähnen den Rahmen sprengen würde, möchte ich Euch herzlich danken.

Meine Freundin Florentina verdient an dieser Stelle noch eine eigene Erwähnung für die Motivation, die Sie mir zukommen ließ, als ich bis spät in die Nacht hinein geschrieben habe und weil Sie sich erbarmte, mir meine Arbeit Korrektur zu lesen, was mir unheimlich geholfen hat. Danke dafür.

Es beschließt sich nun auch meine Studienzeit, die gesamt gesehen eine wunderschöne, wenn auch teilweise nervenaufreibende Zeit darstellte. Mich jedoch erfüllt der Gedanke an ihr Ende mit etwas Wehmut, da ich sie sehr genossen und sie mich zu dem geformt hat was ich jetzt bin.

Und nun, ohne weitere Worte zu verschwenden, wünsche ich viel Spaß beim Lesen.

Maximilian

Abstract

Solid oxide electrolysis cells are used for the creation of fuels for solid oxide fuel cells (SOFC) as well as gases for chemical reactions. The big advantage of the fuel production through fuel cells is the CO_2 neutrality during the creation instead of the use of coal gasification with steam. A main problem we face here is the deposition of carbon on the electrodes which has to be prevented to maintain the usability of the cell. The goal of this work is to test the usability of mixed ionic/ electronic conducting $Cer_{0.9}Gd_{0.1}O_{1.95}$ - cathodes (GDC) on YSZ-electrolyte with LSCF-anodes for CO_2 electrolysis. Furthermore the influence of nickel particles in GDC cathodes was tested and the performance of porous electrodes and thin film electrodes was compared.

Porous electrodes have been screen printed on polycrystalline YSZ substrates with LSCF as counter electrodes and platinum particles as connecting elements. The thin film electrodes are on yttrium stabilized zirconia single crystal (100) electrolytes. The GDC electrodes are applied by pulsed laser deposition (PLD) and the counter electrodes (LSCF) are screen printed and sintered. By impedance spectroscopy the polarisation resistances of all samples could be obtained. The introduction of nickel reduced the polarisation resistances for all samples.

The functionality of the cells was tested by applying direct voltage on the cells. The performances of the cells were compared through the amount of gas produced as well as by the current applied during the measurement. For pure porous GDC-cathodes with a film thickness of $6.9\mu m$ at a voltage of $2V$ a maximum current density of $1.5mA/cm^2$ was obtained. The nickel doping of 10% increased the current density of the GDC layer (film thickness $4.8\mu m$) at the same conditions to $3.7mA/cm^2$. The CO flow corresponds to the current density. In the process pure GDC produced $0.32cm^3$ of CO per minute while doped GDC generated $0.65cm^3/min$. Both had a Faraday efficiency of about 87% during the measurement.

The cells with thin film electrodes showed much better performance with current densities up to $283mA/cm^2$. Reasons for their better performance are possibly poisoning effects due to impurities in the porous electrodes.

Kurzfassung

Als alternative Treibstoffgewinnung für "Solid Oxide Fuel Cells" (SOFC) sowie zur Gewinnung von Gasen für chemische Reaktionen werden bereits "Solid Oxide Electrolyse Cells" (SOEC) eingesetzt. Diese haben den großen Vorteil kein weiteres CO_2 zu produzieren, wie dies bei der Vergasung von Kohlenstoff unter einer Wasserdampfatmosphäre der Fall ist. Die Reduktion von CO_2 geht jedoch mit der Möglichkeit einer Ablagerung von Kohlenstoff an den Elektroden einher.

Das Ziel der Arbeit ist es die Nutzbarkeit von gemischt ionisch/elektronisch leitenden $Cer_{0.9}Gd_{0.1}O_{1.95}$-Kathoden (GDC) auf YSZ-Elektrolyten mit LSCF-Anoden für kontinuierliche CO_2-Elektrolyse zu testen. Weiters soll der Einfluss von Nikelpartikeln in den GDC-Kathoden sowie der Zusammenhang zwischen der inneren Oberfläche der porösen Elektroden und der Dünnschichtelektroden bestimmt werden.

Die porösen Elektroden wurden auf polykristallinem YSZ-Substrat mit LSCF-Anoden mittels Siebdruckverfahren hergestellt und über Platinpartikel kontaktiert. Für die Dünnfilmelektroden wurde ein Einkristall-YSZ (100) als Substrat verwendet, die Arbeitselektrode mittels "Pulsed Laser Deposition" (PLD) aufgetragen und die Gegenelektrode über Siebdruck appliziert und gesintert. Über eine impedanzspektroskopische Charakterisierung der Dünnschichtelektroden stellte sich ein erheblich verringerter Polarisationswiderstand aufgrund einer Beschichtung mittels Nickelpartikeln auf der Oberfläche heraus. Dieser wurde später auch bei porösen Elektroden beobachtet.

Durch Einzelmessungen der jeweiligen Elektrolysezellen wurde die Funktionalität der GDC- sowie Ni/GDC-Kathoden getestet und ein Leistungsvergleich der einzelnen Zellen durchgeführt. An der reinen GDC-Kathode mit einer Schichtdicke von $6.9\mu m$, wurde eine maximale Stromdichte von $1.5mA/cm^2$ bei $2V$ gemessen. Durch eine Dotierung von 10% Nickel und einer Schichtdicke von $4.8\mu m$ konnte die Stromdichte auf $3.7mA/cm^2$ gesteigert werden, wodurch sich mehr als eine Verdoppelung ergab. Der Kohlenstoffmonoxid Produktionsstrom verhielt sich dabei dem elektrischen Strom entsprechend. Undotierte GDC-Kathoden lieferten einen CO-Volumenstrom von $0.32cm^3/min$ während die 10% Nickel dotierten $0.65cm^3/min$ ergaben. Der Vergleich zwischen Dünnfilm und porösen Elektroden ergab einen deutlichen Unterschied der Stromdichten. Bei reinem GDC Dünnfilm konnten sehr hohe Ströme von $283mA/cm^2$ gemessen werden. Gründe hierfür könnten in Degradationen der porösen Elektrode durch Verunreinigung liegen.

Contents

1 Introduction

1.1 Motivation

The production of carbon monoxide primarily happens as a side product of the crude oil refining to produce gasoline. Afterwards this can be used directly as a fuel or for chemical conversion with hydrogen and water or be purified and filled up into gas cylinders for transport. The transport of large amounts of carbon monoxide is problematic due to its toxicity. Therefore there is a strong preference for on-site production of CO to avoid the risks involved with storage and transportation.
Also the production through oil refining is problematic due to the environmental impact of the created exhaust gases during the refining and by using of gasoline. This is a problem which has to be dealt with. Therefore other ways of energy production and also carbon monoxide creation have to be found. A promising technology to fulfil the need of safe and environmentally friendly CO production is electrolysis.
An electrolysis cell is able to reduce carbon dioxide to the monoxide state with the use of electrical current. Also is it able to reverse the reaction to create electrical current. Therefore in case of the need of energy an electrolysis cell for carbon dioxide electrolysis can also be used as a fuel cell. That opens a way to the problematic topic of energy storage. With them, easy accessible chemicals like water or carbon dioxide can be reduced and used as fuels or more reactive chemicals. In case of carbon monoxide the use for Fischer-Tropsch synthesis or Koch reaction is possible while hydrogen is mostly used as a fuel. [35] [23] [6]

Electrolysis reactions:

$$2H_2O \rightarrow 2H_2 + O_2$$
$$CO_2 \rightarrow CO + \tfrac{1}{2}O_2$$

Fischer-Tropsch synthesis:

$$(2n+1)H_2 + nCO \rightarrow C_nH_{2n+2} + nH_2O$$

Koch reaction:

$$C_4H_8 + CO + H_2O \rightarrow C_5H_9OOH$$

Fuel as well es electrolysis cells have the same structure and can be used in both directions. There are different types of fuel cells which have been developed by now. They differ by various operating temperatures, electrolyte materials and used fuels. The fuel cells can be divided in classes due to their electrolyte. The lowest operation temperature of all fuel cells ($80°C$) have polymer electrolyte membrane fuel cells (PEMFC) which have a proton conductive electrolyte and are already used, for example, for small devices like cars or boats. The biggest disadvantage is their vulnerability to carbon monoxide poisoning why only pure hydrogen can be used as fuel. Another fuel is used in a special type of PEMFC which is methanol and this is called direct methanol fuel cell (DMFC). Although the efficiency of a DMFC is only at about 30% instead of 50% which the PEMFC reaches, the use of a liquid fuel is an advantage in handling and storage. Alkaline fuel cells use potassium hydroxide as electrolyte are used between $60°C$ and $120°C$ but have a shorter durability due to their corrosive electrolyte and suffer like PEMFC from carbon dioxide poisoning. High temperature fuel cells are molten carbonate fuel cells (MCFC) which are used between $600°C$ and $700°C$ and solid oxide fuel cells (SOFC) which are used between $700°C$ and $900°C$ and are unsusceptible to carbon monoxide and dioxide. [38]

For the use of carbon dioxide electrolysis SOFCs seem in reverse operation mode to have the best properties and is in general known to be a promising technology especially because of the fact that carbon monoxide can be used as fuel in the fuel cell mode. They operate with different fuels and can be coupled with heating systems. To further improve the efficiencies and to deal with known problems like sulphur poisoning and stability problems on long term use its essential to study new electrode- as well es electrolyte materials. [24]

1.2 Aim of the current work

Current research about CO_2 electrolysis often deals with different perovskite-type electrodes like (La,Sr)$CrO_{3-\delta}$ or electrodes based on doped ceria like $Sm_{0.2}Ce_{0.8}O_{1.9-\delta}$. Fuel cells with gadolinium doped cerium oxide-cathodes are currently mostly used with hydrogen and for water electrolysis.

The usability of such electrodes also for CO_2 electrolysis has to be verified and the forming of carbon on the surface has to be prevented. The influence of the doping of nickel, which is typically done when employing these electrodes in fuel cells, will be verified during electrolysis. By electrical impedance spectroscopy electrochemical properties like their polarisation resistance will be measured. The main measurements are done with porous electrodes. To determine the active surface, the area specific resistance as well as the power output per area have to be observed through the use of thin film electrodes with well defined geometries. One main goal is the production of a ratio of at least 4% carbon monoxide in carbon dioxide to be able to use the exhaust for chemical reactions without refining it first. In the end the durability of the electrodes have to be investigated to see the degradation during the measurement time.

2 Theory

2.1 Defects in solids

Typically ceramics are featured as highly structured lattice in regard to their crystallinity and periodicity. Even more than the structure of the perfect state, the defects in their structure are the key to their electrical and mechanical properties. For explanation, the autoprotolysis of water, which is pivotal for its conductivity, can be chosen as an analogy. Water forms small amounts of H_3O^+ and OH^- ions within the water. If the water is now subtracted from it like Figure 2 shows, the excess H^+ can be seen as a defect and the missing H^+ as a missing OH^- or a proton vacancy. [21]

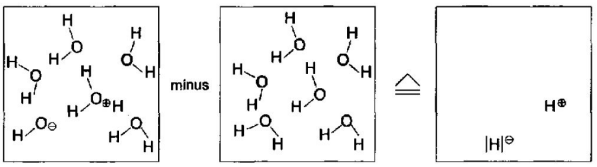

Figure 1: Protonation of H_2O. Water transfers hydrogen ions to another water molecule and produces through that imperfections. Reprinted from [21]

To determine the effects of defects on the properties of ceramics, the different kinds of defects have to be distinguished. The first recognised defect was the point defect which can be divided in ionic and electronic point defects (0 dimensional). Further higher dimensional defects such as linear defects (1 dimensional), planar (2 dimensional) and volume defects (3 dimensional) have been identified. While linear defects mostly explain the mechanical properties, planar as well as volume defects have important roles for many physical and chemical properties. The electronic properties and ionic conductivity are mostly given through point defects of the materials and grain boundaries.

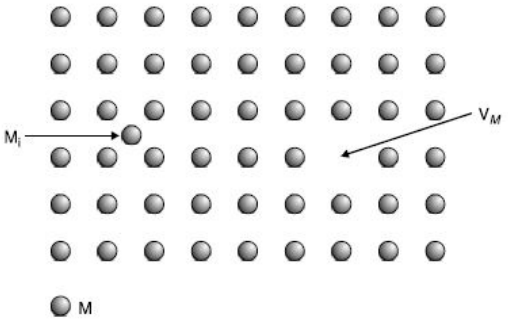

Figure 2: Point defects in a single elemental crystal, M stands for the element, V_M a vacancy and M_i an interstitial. Reprinted from [42]

There are different types of point defects. The simplest is a substitution of an atom with an atom of another element in the crystal lattice. Another one would be an interstitial atom incorporated into the structure. Due to the fact that there is not enough space for another atom, the lattice is distorted around the interstitial atom to make enough space.

The third point defect is a vacancy, which means a hole in the structure due to a missing atom.

To display point defects the Kröger-Vink notation is usually used for generalized point defects and reads:

$$Particle(A)^{relativ\ charge(C)}_{site(B)} \tag{1}$$

Here A indicates the atom in the certain position and is stated with the chemical symbol of the impurity. In case of a vacancy the letter V is used. The replaced atom or ion in that position is labelled with B and the relative charge with C. In case of an ideal material, the abbreviation nil displays a defect less crystal site.

In the Kröger-Vink notation only relative or effective charges are considered. The relative charge composes of the charge of the new ion, subtracted by the charge of the substitutes in the position. Effective positive charges are indicated with a superscript dot ($^\bullet$), negative charges with superscript of a vertical stroke (') and neutral charges with an x. For example, a vacancy in NiO on the oxygen site the symbol $V_O^{\bullet\bullet}$ would be used. Sr^{2+} on the place of La^{3+} would be called Sr'_{La} and Mn^{3+} at the site of Cr^{3+} would be Mn^x_{La}. Interstitial sites, due to the fact that they are normally unoccupied in the perfect state, don't have a pre-existing charge. Therefore the real charge of the ion is the same as the relative charge. The interstitial defect of Zn^{2+} in a crystal is given with the symbol $Zn_i^{\bullet\bullet}$. Beside ionic defects electronic defects, which are negatively charged electrons and positively charged electron holes, play an important role. In Kröger-Vink notation, they are described as e' and $h^\bullet$. Unbalanced concentrations of positively and negatively charged defects would lead to an overall charge of the crystal. Since materials are charge-neutral on a macroscopic scale each defect has to be opposed with another defect to keep the total charge neutral. These intrinsic defects in ionic ceramics arise as paired defects and are classified in Schottky defects where every cation vacancy is opposed with an anion vacancy (V_{cation}, V_{anion}), Frenkel defects where interstitials lead to a vacancy of the same charge (V_{cation}, $Cation_i$) and Anti-site defects (A'_B, $B^\bullet_A$). On Anti-site defects atoms of different elements in the site are substituted. That lets the total charge untouched but leads to a bending of the crystal due to the different size of different element atoms. In ceramic materials, these defects operate as charge carriers and can be formed within the material through a rise of the entropy of the system (intrinsic charge carriers) or by

doping with another material (extrinsic charge carriers). [42]

The only way to observe theoretically an ideal crystal without defects would be at $0K$. As soon as the temperature rises the influence of the entropy leads to a forming of defects. These intrinsic defects are in an equilibrium at each temperature. The amount of intrinsic charge carriers increases with the temperature and so does the conductivity as well. For undoped materials these intrinsic charge carriers provoke the electronic and ionic conductivity. The same effect can be accomplished by extrinsic charge carriers which are introduced by doping of the ceramic. The concentration of defects due to doping is independent of temperature. Through doping, ionic and electronic defects can be introduced into a material. [43] [34] [16]

2.2 Electrochemical reactions

Electrochemical reactions describe the exchange of electrons in the process of a redox reaction and can generally be written as:

$$A_{ox} + B_{red} \rightarrow A_{red} + B_{ox}$$

This reaction can now be split in two half reactions:

$$\text{Reduction: } A_{ox} + ne^- \rightarrow A_{red}$$
$$\text{Oxidation: } B_{red} \rightarrow B_{ox} + ne^-$$

The amount of electrons ($n\ e^-$) depends on the charges of the reactants. As an example the reaction of CO to CO_2 can be used:

$$\text{Reduction: } \tfrac{1}{2}O_2 + 2e^- \rightarrow O^{2-}$$
$$\text{Oxidation: } CO + O^{2-} \rightarrow CO_2 + 2e^-$$

$$\text{Reaction: } CO + \tfrac{1}{2}O_2 \rightarrow CO_2$$

The amount of electrons released through the oxidation reaction are consumed in the reduction reaction. To be able to use the electron flow as an electric current, the half-cell reactions have to be separated spacially. The oxidation happens on the anode and the reduction on the cathode. These have to be connected through an external circuit to keep the reaction going. In order to prevent a charging of the half cells due to the one sided electron flow, which would induce a difference in the electric potentials, an electrolyte which separates and connects the electrodes is needed. This enables an ion flow to compensate the electric current. The electrolyte can be a salt bridge or a semi-permeable membrane for certain ions. The generated open circuit voltage is then a matter of the electrochemical potentials of the used reactants. An electrochemical cell which is used to obtain an electrical current is called galvanic cell (i.e. batteries, fuel cells). For the determination of the possible voltage of an electrochemical cell the thermodynamics of the cell have to be taken in account. A reaction only happens if the change of free enthalpy is negative ($\Delta G < 0$). The change of free enthalpy can be calculated with:

$$\Delta G = \Delta H - T\Delta S \tag{2}$$

with:

ΔG	free enthalpy change [J/mol]
ΔH	enthalpy change [J/mol]
T	absolute temperature [K]
ΔS	entropy change [J/mol*K]

The first principle of thermodynamics states the constants of energy. Therefore electrical and chemical energy can be set on an equivalent level.

$$W_{chem} = \Delta G = \Delta H - T\Delta S \tag{3}$$

$$W_{el} = Q * U = z * F * U_c \tag{4}$$

with:

W_{chem}	Chemical work [J/mol]
W_{el}	Electrical work [J/mol]
Q	Charge [C]
U	Voltage [V]
z	Electrons being transferred []
F	Faraday constant [C/mol]
U_c	Open circuit voltage [V]

They can be combined to:

$$W_{chem} = -W_{el} = \Delta G = -z * F * U_c \tag{5}$$

And the open circuit voltage of a chemical reaction can be calculated with:

$$U_c = -\frac{\Delta G}{z * F} \tag{6}$$

Depending on the half cell reactions a certain voltage can be achieved. The theoretical voltage of a half cell is possible to be determined over the potentials in the standard electrode potential series. The standard electrode potentials show the potentials of half cell reactions with a hydrogen half cell as counter electrode which is defined with $0V$. [7] [10]

2.3 Solid oxide cells (SOC)

Solid oxide cells represent high temperature solid oxide fuel cells (SOFC) as well as solid oxide electrolysis cells (SOEC). A solid oxide cell is an energy conversion device which is able to produce electrical energy (and heat) out of fuel and oxidant, or fuel and oxidant through electrical energy. A fuel cell consists of an electrolyte which separates two electrodes (anode and cathode) as well as connectors to build up an external circuit. In case of a fuel cell, the fuel is transported to the anode where it is oxidised to release electrons to the external circuit. The oxidant is lead to the cathode to be reduced by electrons supplied by the external circuit and the species travel through the electrolyte to the anode. This electron flow leads to an electric current in the external circuit. Due to the low voltage per cell, in technological devices many fuel cells are bound together in stacks with interconnects between the cells that separate cathode from anode gases and electrically connect the cells. Electrolysis cells work the other way around. Therefore an external electron source is necessary and molecules like water or carbon dioxide have to be supplied to the cathode. Thus they dissociate and the formed anions (O^{2-}) travel through the electrolyte to the anode to be reduced (see Figure 3). [27] [28]

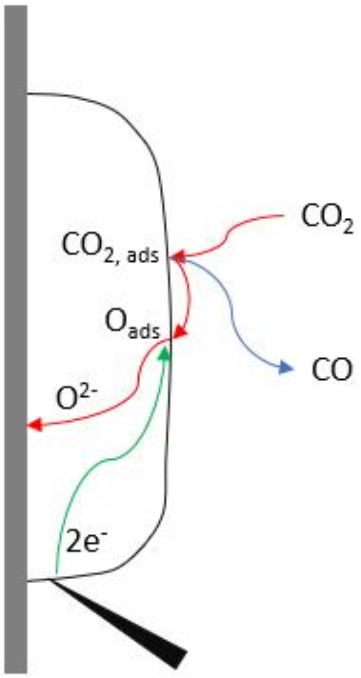

Figure 3: Pathway of molecules and ions at a mixed conducting cathode of a SOEC on the example of CO_2 electrolysis. CO_2 diffuses to the cathode and adsorbs on its surface. Then CO and O separate. O is reduced with externally supplied electrons to form O^{2-} and travel to the electrolyte and finally to the anode.

An electrolyte should have a very high electronic resistance to prevent internal short circuit and a very high ionic conductivity. The most commonly used electrolyte is yttria-stabilized zirconia (YSZ).

Both electrodes need to be good ionic as well as electronic conductors. The ionic conductivity improves the electrode kinetics due to the possibility of the ions not only to reach the electrolyte via triple phase boundary but also to open the bulk path. Further requirements of the electrodes are a stability under different oxygen partial pressures, thermochemical stability and a high catalytic activity for the desired reaction. [33]

According to that, oxygen has to be reduced to be able to travel through the electrolyte in a fuel cell and therefore there are two possibilities. The first would be over the surface of the electrode particles and the second is through the bulk path. [31] [32]

For the first option, oxygen has do be absorbed on the electrolyte particle and dissociates there. Afterwards a diffusion on the surface towards the triple phase boundary is necessary where the electrolyte meets the electrode and the gas phase. On that point the oxygen gets reduced to O^{2-} and is incorporated in the electrolyte. This process is sketched in Figure 4a). This pathway dominates primarily for electrodes with a low ionic conductivity like LSM in air or Pt and Ni.

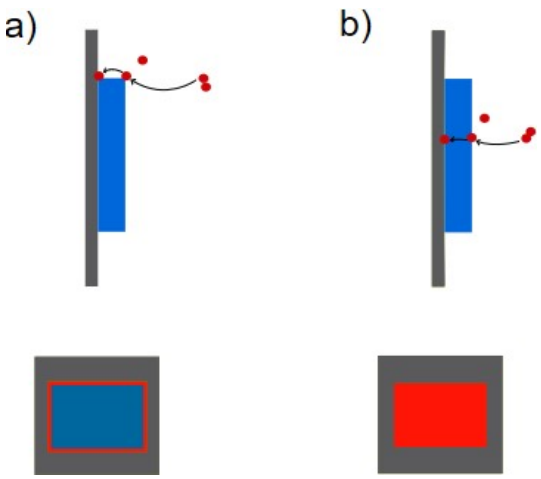

Figure 4: Different ways of incorporation of oxygen into the electrolyte in SOFC cathodes. The electrode is shown in blue and the electrolyte is grey. The active area of the reduction reaction is shown in red in the lower pictures. a) A material with low ionic conductivity which is active on the tripple phase boundary; b) A material which enables the bulk path and is active on the whole surface

The second option is through the bulk of the electrode material. Therefore oxygen is absorbed and dissociated in the same way as in the first method. But instead of travelling on the surface, the oxygen is reduced right at the spot and the ion is then incorporated into the electrode where it travels through to the electrolyte which is sketched in Figure 4b). Therefore the electrode has to be a mixed ionic electronic conductor like gadolinium doped cerium oxide. The big difference between these two ways is the amount of active material. While on the first way only the edge of the electrode is involved in the reduction, the whole area of the electrode is active in the second way which increases the performance a lot. [5] [13] [15] [45]

2.4 Ceramic materials

Ceramics are solid inorganic materials consisting of metals and non metals in ionic and covalent bonds and mostly are oxides, nitrides or carbides. Per definition of the German Ceramic Society, ceramics are an *"inorganic, non metal, water slightly soluble and at least 30% crystaline"*[19], which keeps glasses out of the group of materials.[19]
Their main mechanical properties are hard, brittle, strong in compression, weak in shearing tension and resistant to high temperatures. In a chemical point of view they are mostly inert to acidic reaction and reactions in high temperatures. The properties depend on the used materials as well as their microstructure, density, grain size distribution, defects and second phases. They can be from amorphous over semi-crystalline to a highly oriented crystalline state. Many ceramics are insulators but their properties can be changed to conducting. There are different ways to categorise ceramics.
One is to divide them into three material categories which are oxides (e.g. alumina, zircon, ceria), non-oxides (e.g. carbide, boride, nitride, silicide) and composite materials (e.g. fiber reinforced, particulate reinforced, combination of oxides and non-oxides). Another way to categorise them is into traditional ceramics which are used for their mechanical properties and advanced ceramics which are further separated into electroceramics and advanced structural ceramics. Electroceramics exhibit special dielectric, magnetic, optical or conductive properties. Advanced structural ceramics are made to have a biocompatibility or to withstand very high mechanical influences. [16] [11]

2.4.1 LSCF

Lanthanum strontium cobalt ferrite ($La_{0.6}Sr_{0.4}Co_{0.2}Fe_{0.8}O_{3-\delta}$) (further called LSCF) is a ceramic oxide containing lanthanum(III)oxide, strontium oxide, cobalt oxide and iron oxide. The material has a high concentration of electronic defects and oxygen vacancies which leads to the properties of a mixed ionic electronic conductor (MIEC) with a high electronic conductivity. [39] [40]
The main structure of a perovskite can be generalised with ABX_3 which is the same crystal structure as $CaTiO_3$. While there are large atoms to form the lattice on the A site, the site of B is occupied with small atoms. Lanthanum and strontium is on the A site, ferrite and cobalt occupies the B site. A and B present the cations while X represents the anion and is an oxide in that case.

In Figure 5 the crystal structure of a perfect cubic perovskite lattice is shown. The blue spheres represent 'A' cations, black spheres 'B' cations and red spheres anions (X). A wide variety of cations is able to form perovskite structures. Due to this compositional diversity a large variety of different properties like electronic conductivity, ionic conductivity, catalytic activity and magnetism can be achieved. These properties can also be adjusted through doping of the crystal. This encourages to develop electrode materials with perovskite structure furthermore.

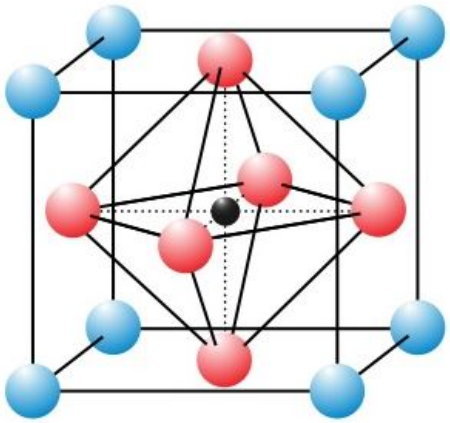

Figure 5: Schematic perovskite crystall structure. A is represented with red, B in the center wih black and X with blue on the corners. Reprinted from [1]

For perovskite materials the oxygen partial pressure in the atmosphere is important for their conductivity. This is due to the fact that the perovskite type oxide is in an equilibrium with the surrounding atmosphere. Thereby the defect chemistry of the material depends on the oxygen partial pressure:

$$O_O^x \rightleftarrows \frac{1}{2}O_2 + V_O^{\bullet\bullet} + 2e' \tag{7}$$

Electrons and holes recombine ($h^\bullet + e' \rightleftharpoons nil$) and accordingly an equation equivalent is:

$$O_O^x + 2h^\bullet \rightleftarrows \frac{1}{2}O_2 + V_O^{\bullet\bullet} \tag{8}$$

With the oxidation of oxygen ions, electron holes are consumed. A lower p_{O_2} decreases the conductivity. [37] [22]

2.4.2 GDC

Gadolinium-doped cerium oxide ($Ce_{0.9}Gd_{0.1}O_{1.95}$) (further called GDC) crystallises in a cubic fluorite structure like pure cerium oxide does as well [41]. The generalised structure can be written with AX_2. On the A spite is cerium, partly replaced with gadolinium. The X site is occupied with oxygen. The A atoms form a cubic face-centred structure. Each A ion is surrounded with a cube of 8 X ions while each X ion is surrounded by 4 A ions tetrahedral. The integration of gadolinium(III) on sites of cerium(IV) leads to oxygen vacancies and furthermore to a high ionic conductivity of the material. [41]

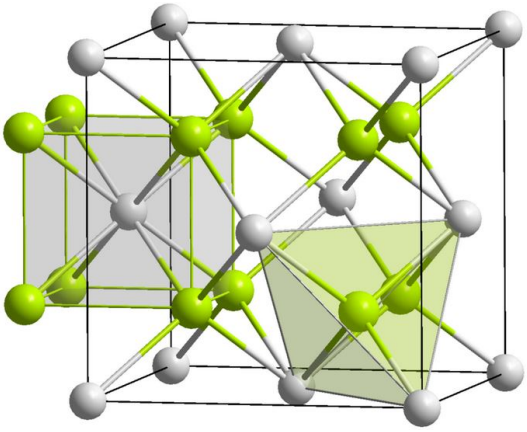

Figure 6: Schematic cubic structure with grey spheres for kations and green spheres at the anion places. Reprinted from [3]

Doped ceria is a well researched electrode material due to its good catalytic properties, substantial oxygen conductivity and phase as well as thermal stability. It is a good ionic conductor and in reducing atmosphere also a good electronic conductor. A reason for the catalytic activity is the presence of a Ce^{4+}/Ce^{3+} redox couple which has to be induced because pure ceria has no oxygen vacancies which makes it a poor ion conductor. [25] The ion conductivity in ceria is induced through a vacancy diffusion mechanism. In reducing atmosphere and at temperatures above $700°C$ ceria tends to reduce from Ce^{4+} to Ce^{3+} which results in the formation of oxygen vacancies and additional electrons as charge compensation. This can be shown through the following defect reaction in Kröger-Vink notation: [20]

$$2Ce_{Ce}^{x} + O_{O}^{x} \rightarrow \frac{1}{2}O_2 + 2Ce'_{Ce} + V_{O}^{\bullet\bullet} \tag{9}$$

These electrons are located at Ce ions, forming small polarons Ce'_{Ce}. If these polarons then migrate through the lattice, electronic conduction is enhanced.

Another way to induce oxygen vacancies to improve the oxygen ion conductivity is through partly substitution of Ce^{4+} with cations of another oxidation state. [30] [17]

$$Gd_2O_3 \xrightarrow{CeO_2} 2Gd'_{Ce} + 2O_{O}^{x} + V_{O}^{\bullet\bullet} \tag{10}$$

2.5 Boudouard equilibrium

The Boudouard reaction describes the equilibrium between carbon dioxide (CO_2) and carbon monoxide (CO) which forms through glowing carbon in an oxygen atmosphere.

$$C_s + CO_{2,g} \rightleftharpoons 2CO_g \qquad \Delta G_{800°C} = -23.2\frac{kJ}{mol} \tag{11}$$

The enthalpy of formation of carbon dioxide is $\Delta H_f^0 = -393.5kJ/mol$ [29] and of carbon monoxide $\Delta H_f^0 = -110.5kJ/mol$ [29]. This leads to an exothermic reaction for the formation of carbon dioxide. Although the formation enthalpy of carbon dioxide is far higher than the one of carbon monoxide, the formation entropy is much lower ($\Delta S^0_{f\_CO_2} = 213.6J/mol$ [2], $S^0_{f\_CO} = 198.0J/mol$ [2]).

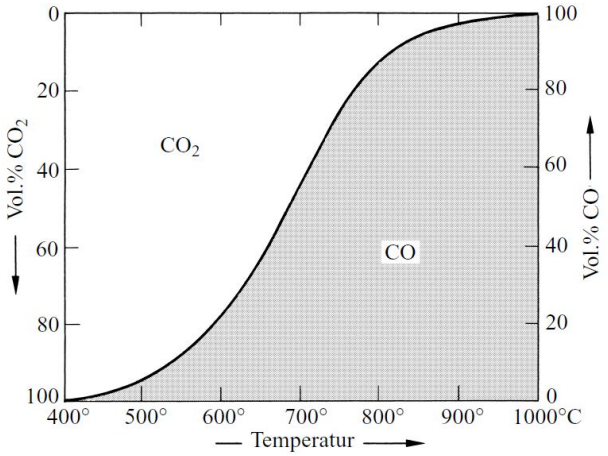

Figure 7: Influence of the temperature at atmospheric pressure on the formation of CO and CO_2. At $1000°C$ the Boudouard equilibrium is reached an CO_2 reduces automaticly in the presence of carbon. Reprinted from [29]

This leads to the outcome that the standard free energy of formation of carbon dioxide is nearly independent of the temperature while the formation energy of carbon monoxide decreases with increasing temperature. At about $400°C$ the equilibrium is at the side of carbon dioxide, while at $1000°C$ its nearly completely on the carbon monoxide side, considering atmospheric pressure as displayed in Figure 7. At the main temperature of $800°C$ the standard reaction enthalpy (ΔG) is already negative which leads to a reaction to the CO side (see equation 11).

Beside the temperature also the pressure is a factor to influence the equilibrium. The increase of gas molecules at the formation of carbon monoxide can be promoted through decreasing pressure. In a carbon free atmosphere with an oxygen excess the ratio of CO to CO_2 in no longer dependent of the Boudouard equilibrium but from the dissociation equilibrium of CO_2:

$$283.17kJ + CO_{2,g} \rightleftharpoons CO_g + \frac{1}{2}O_2 \tag{12}$$

Even at higher temperatures, up to about $700°C$, the equilibrium is almost completely at the side of CO_2 and can only be influenced through a supply of energy to break the bonds. To keep carbon monoxide permanently stable, the oxygen has to be removed to

prevent the reverse reaction. Although there is no carbon in fuel cells from the beginning, it forms partly on the triple phase boundaries. Thus carbon reacts furthermore with CO_2 to fulfil the equilibrium. [29]

2.6 Faraday effeciency

The Faraday efficiency (or Coulomb efficiency) describes the efficiency of the electrical energy, which is used to carry out a chemical reaction. For the calculation of the efficiencies of the cells the received currents I were compared to the theoretical minimum current I_{theor} necessary for the production of the actual produced CO amount. Given set-up values for the calculation were the flow rate of CO_2 $\dot{V}_{CO_2}$, the percentage of CO in the exhaust ω_{CO} and the measured current I. Furthermore the measurement temperature $T = 298K$, the atmospheric pressure $p = 101300Pa$, the Faraday constant $F = 96485C/mol$, the universal gas constant $R = 8.314J/mol*K$ and the charge number $z = 2$ were used. First the flow rate of CO $\dot{V}_{CO}$ was calculated with:

$$\dot{V}_{CO} = \frac{\dot{V}_{CO_2} * \omega_{CO}}{100} \tag{13}$$

Through this the chemical amount of CO n_{CO} could be calculated with the ideal gas law:

$$n_{CO} = \frac{p * \dot{V}_{CO}}{R * T} \tag{14}$$

Furthermore the theoretically required current can be calculated with:

$$I_{theor} = z * n_{CO} * F \tag{15}$$

And in the end the Faraday efficiency F_e is the quotient of the theoretical to the observed current and should be between 0 and 1. [14] [46]

$$F_e = \frac{I_{theor}}{I} \tag{16}$$

2.7 Measurement

2.7.1 Single gas test bench

For the categorisation of SOFC electrodes with thin film electrodes and symmetrical electrodes, a single gas test bench was used. The test bench's centre is a horizontal quartz bar. On its outer end is a platinum sheet to contact the lower electrode of the cell while it lays on it. To contact the micro-electrodes, vertical platinum needles are mounted on the outer end of two quartz tubes which are attached moveably on the front of the test bench. The platinum sheet as well as the needles are connected separately via platinum wires to the connectors on the front part. The set-up is made with two wires for cathode and anode to enable a four point measurement to eliminate the resistance of the cable which is used for measurement.

To get a stable atmosphere around the sample, a quartz cylinder which is closed at the outer end and leak proof connected on the front side. To reduce the influence of the induction of the heating element, a steel mesh is mounted around the quartz cylinder. The heating is carried out with a horizontal moveable electronic furnace. Furthermore a type S thermocouple is installed below the specimen holder for the in-situ measurement of the temperature. The voltage is applied with a potentiostat/ galvanostat which is also used to measure the resulting current as well as the impedance spectra of the sample. The received data is then evaluated with a computer software (Javalab AC 15; Winchem 1627-3).

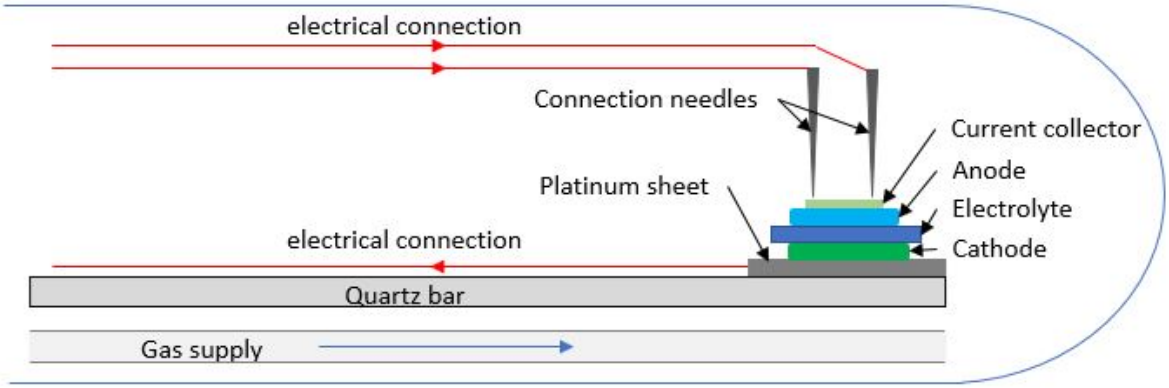

Figure 8: Schematic picture of the single gas test bench. Voltage is applied through connection needles onto the platinum mesh. The porous cathode is placed on a platinum sheet to close the electrical circuit. A quartz pipe below the support bar is used to supply the used gas.

When electrolysis is performed in a single chamber test bench, CO and O_2 are released into the same gas chamber, leading to an imperfectly defined atmosphere. Only when the rate of O_2 "pumping" is small, compared to the rate of CO_2 reduction, the electric current can be correlated to the reduction rate. For this reason, micro-electrodes with $1.4mm^2$ were used, which deliver a maximum total current of $4.7mA$, corresponding to a O_2 release rate of $0.003cm^3/min$ at the bottom electrode. Due to the constant flow CO_2 of $100cm^3/min$, the total concentration of formed O_2 did not exceed $30ppm$. This concentration is similar to the estimated $10 - 100ppm$ in the inlet gas, whereby no major influence of O_2 "pumping" can be expected.

2.7.2 Dual gas test bench

The test bench set-up is made to measure the test cell with two different gases on the anodic and cathodic sides. Therefore an alumina oxide tube is standing vertically on the base on which the cell is mounted and sealed with a glass sealant. It keeps the atmosphere inside the tube separated from the outer atmosphere. A quartz glass cylinder with a closed end encloses the chamber.

The heating is carried out with a vertically moveable tube furnace to be mounted and unmounted over the quartz cylinder to enable a way to exchange samples. The feed pipes are made out of chromium steel and the exhaust pipes are out of nickel free chromium steel to prohibit the formation of nickeltetracarbonyl ($Ni(CO)_4$) which is very toxic, flammable and dangerous for the environment. The electrode which is placed on the alumina tube is sealed with a Duranglas ring (thickness 1mm) that melts partly during the heating process and tightens up against gas leaks. To ensure the impermeability of the sealing, the electrolysis cell is also weight down with a 200g alumina oxide component from above. The connection is carried out with platinum wire.

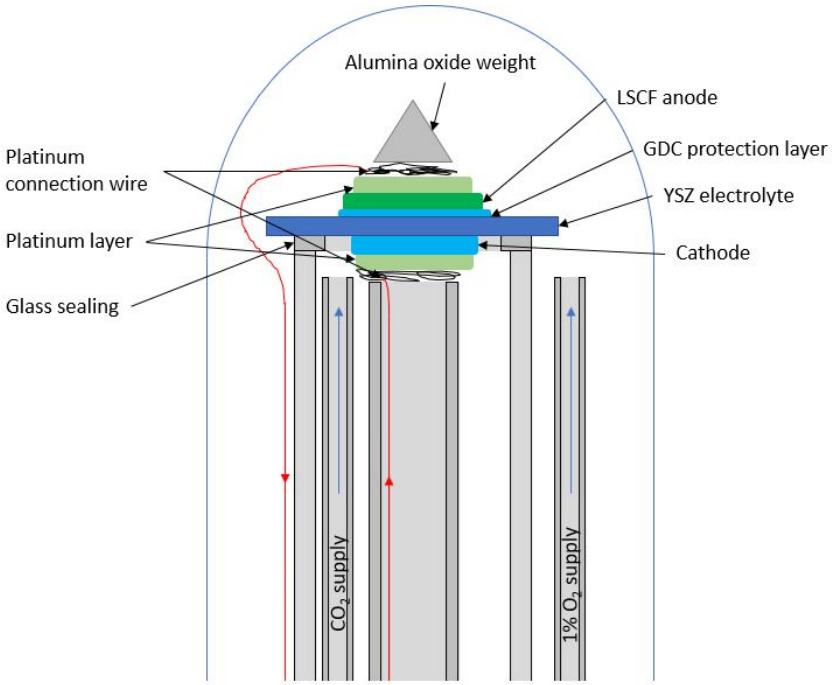

Figure 9: Schematic sample restraint of the dual gas test bench. The dark blue electrolyte is placed on the glas ring. The GDC-cathode is shown in light blue and the LSCF-anode in green. The connecting platinum layer is presented in mud green.

The connection of the upper electrode is enforced with the applied weight and a space holder out of platinum to improve the gas flow on the upper side. For the inner electrode another alumina tube on a spring with the platinum wire on the upper end is placed inside the first tube and presses the wires against the electrode. Each contact point on the electrodes has two separate supply cables to enable a four point measurement. The gas supply is led from the base directly up to the electrodes with $2mm$ alumina tubes and the exhaust is collected separately for the inner and outer gas room on the bottom of the chamber. A type S thermocouple is installed in the outer gas room for an in situ temperature measurement. The exhaust of the inner gas chamber is then carried to a mass spectrometer to analyse the result of the measurement. The voltage is applied with a potentiostat/galvanostat which is also used to measure the current as well as the impedance spectra of the sample. The received data is then evaluated with a computer software (Javalab AC 15; Winchem 1627-3).

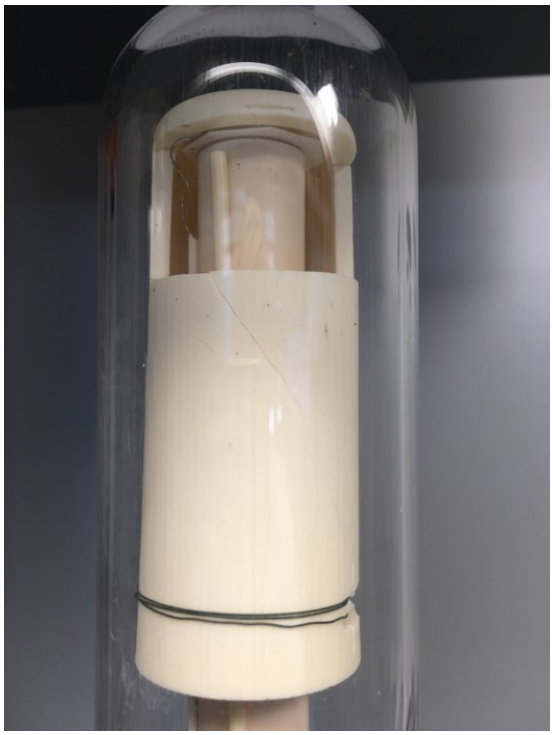

Figure 10: Picture of the sample restraint with a mounted cell.

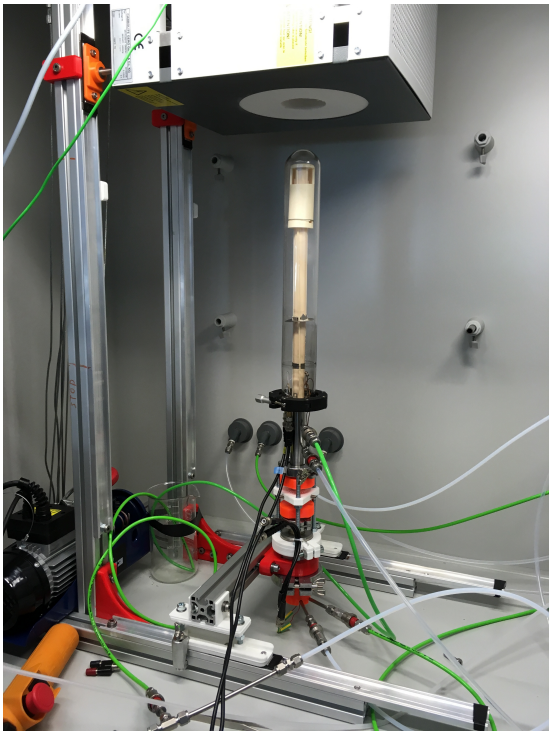

Figure 11: Picture of the used test bench with the furnace lifted on the top.

2.7.3 Mass spectrometry (MS)

Mass spectrometry is a measurement process to separate ions based on their mass to charge ratio. To be able to separate chemical substances for that purpose they have to be in a gaseous state. Liquid samples have to be vaporised before injection. The created gaseous jet first needs to be ionized. This is possible through ion bombardment, laser ionisation, chemical ionisation, an electric field or some further methods. The required energy for the ionisation is called the ionisation energy. If there is more energy available as needed for the ionisation, molecules start to break into charged fragments. These fragments later separate in a different way than the intact ionised molecules because of their lower mass, which leads to results of molecules which are not present in the sample. For the separation, ions are accelerated through a weak electrical field and a potential gradient after it. The speed of the ions differ depending on the acceleration voltage of the field U, the mass of the ion m, the elementary charge e as well as their charge number z.

$$zeU = \frac{mv^2}{2} \tag{17}$$

The moving ions are separated after this step due to their mass. This is possible over the time the ions need to travel after the acceleration through a pipe. Ions with lower masses are faster and can be detected earlier. Other methods are through deflection with a magnetic induction inside a magnetic field, an electric field in a quadrupole mass spectrometer or some other methods of minor importance.

The detection is possible in three different ways. The first one is the detection of ions with different deflection radii with a photo plate or a secondary electron multiplier detector. The second possibility is to set multiple receivers in different positions, so that only ions with a specific deflection angle reach one of them. Impacting ions transmit their charge to them which can be detected. The last method is the mount of a collector slid which only allows ions with a certain bending radius to reach the receiver. To measure different ions the voltage or strength of the magnet field is varied which alters their bending radius.

To identify the different species, the detected masses can be compared to standard series or as a match of the fragment pattern with known characteristic fragment patterns. For practical application this means that the MS signal depends on ionisation cross section times concentration of detected ions and that peaks belonging to fragments (CO in case of CO_2 carrier gas) will always appear, which complicates quantification of the CO_2 concentration and requires calibration. [9] [18]

2.7.4 Electrochemical impedance spectroscopy (EIS)

Generating a physical-chemical model for fuel cells can help to separate the total polarization resistance of the cell in anode, cathode and electrolyte contributions. This helps to identify the rate limiting components. Therefore the processes responsible for polarisation and through that an decrease of their performances have to be identified. Electrochemical impedance spectroscopy (EIS) gives insight into the complex SOFC system where chemical reactions and transport processes can be modelled with an equivalent circuit model.

EIS is an electrochemical characterisation method where an alternating current i(t) with a modulation amplitude i_0 and a frequency f is applied. The resulting voltage u(t) has the same sinusoidal course but the amplitude u_0 is different and phase shift takes place. The outgoing signal is then used to calculate the impedance which is the complex electrical resistance. This is shown in equation 18 until equation 20.

$$i(t) = i_0 \; sin(\omega t + \varphi_I) \tag{18}$$

$$u(t) = u_0 \; sin(\omega t + \varphi_U) \tag{19}$$

$$\underline{Z}(\omega) = \frac{u(t)}{i(t)} \tag{20}$$

A transformation enables the plot in the complex plane (see equation 21).

$$\underline{Z}(\omega) = \frac{u_0}{i_0} \; e^{i(\omega t + \varphi)} = Z'(\omega) + i \; Z''(\omega) \; = Re(\underline{Z}) + i \; Im(\underline{Z}) \tag{21}$$

For SOFC commonly the impedance spectroscopy is carried out from 10mHZ to 1MHz with an used amplitude from 2 up to 10mV. For characterisation the course of the impedance $|Z|$ and the phase shift φ is plotted over the angular frequency ω in a Bode diagram or with a Nyquist plot with imaginary $Im(Z)$ over real part $Re(Z)$. [12] With the help of a equivalent circuit diagram the empirical measurement information can be separated due to their electrochemical processes in the fuel cell and can be pictured with electronic equivalents like resistance, capacity and induction. Through this models ohmic and polarisation resistances can be obtained. The equivalent circuit diagram mostly consists of different interconnected impedance elements like resistors, capacitors or inductors. The electronic parts in the equivalent circuit just represent the real electrochemical processes in the fuel cell. As it is the case for simple electrode geometries the impedance of the different parts of the diagram can be added together like it is shown in figure 13. [44]

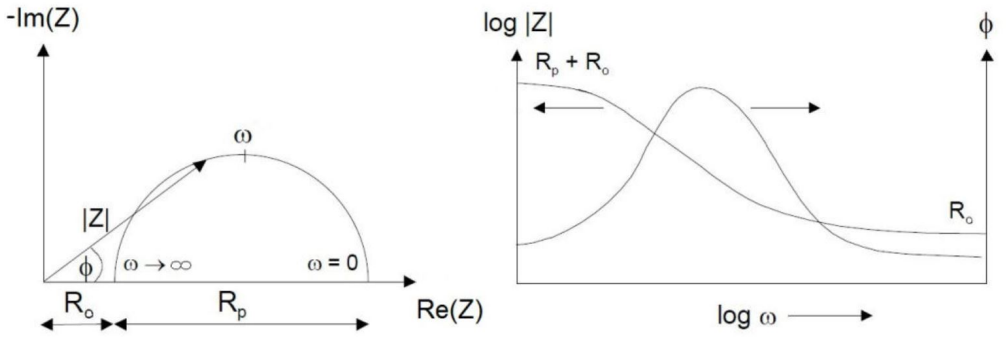

Figure 12: Schematic Nyquist and Bode diagram of an RC circuit. The Bode diagram is a integration of the Nyquist plot. $\omega \to \infty$ is at high frequencies, $\omega \to 0$ is at low frequencies. On the real axis is the resistance of the set-up and wires (R_0) and the polarisation resistance R_P shown. Reprinted from [4]

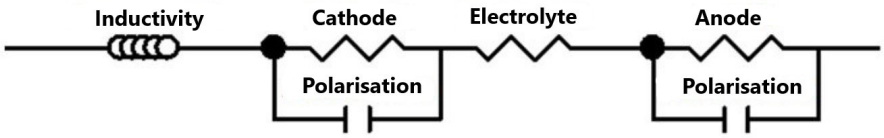

Figure 13: Equivalent circuit diagram for an SOFC which models electrode polarisation, electrolyte resistance and wire resistance. Reprinted from [4]

An ideal ohmic resistor R_Ω is characterised through frequency independence and a phase shift of $0°$ and has therefore a real part.

$$Z_(\omega) = R_\Omega \tag{22}$$

In the equivalent circuit diagram the ohmic resistance represents wire resistances as well as contact resistances on the interface but is normally dominated by the electrolyte resistance. With high ionic conductivity and moderately hight frequencies the inductive as well as the capacitive resistance of the electrolyte is negligible which enables the graphic evaluation to separate the electrolyte resistance from the electrode polarisation. In the Nyquist plot the intercept on the x axis is the ohmic resistance R_Ω which is on $\omega \to \infty$ like it is pictured in figure 12. At $\omega = 0$ the intercept shows the intersection point of the polarisation resistance and the whole resistance. Impedance of ideal capacitors happens through loading and discharging. In real systems they are approximated through RC elements. The electrochemical process is contingent on the frequency dependent time constant τ. Above a certain frequency the time is too short to load and at frequencies of $\omega \to \infty$ the current flows almost only over the capacitance which is shown in equation 23 until equation 25. On the other hand at low frequencies $\omega \to 0$ the current flows mostly

over the resistance element.

$$\omega = 2\pi f = \frac{2\pi}{\tau} \rightarrow \tau = \frac{1}{\omega} \tag{23}$$

$$\tau = RC \tag{24}$$

$$\omega >> \frac{1}{RC} \rightarrow Z_{RC} = -i\frac{1}{\omega C} \tag{25}$$

Real systems normally differ from ideal behaviour because of their three dimensional structure of their electrodes. To model non-linear behaviour of electrode processes constant phase elements (CPE) are used which show non ideal capacitors to approach the real system. The impedance of the CPE elements is called Z_{CPE} and is defined with: [12]

$$Z_{CPE} = T^{-1}(i\omega)^{-P} \tag{26}$$

T is in this case a coefficient and equals the reciprocal impedance at the angular frequency $\omega = 2\pi f$. P can take every value between 0 and 1, and shows an ideal capacitor at 1 and a pure resistor at 0. The values given by the software for CPE elements are T and P. While P is a factor which states how good the approximation of a capacitor is (1 for a pure capacitor), T is a factor to calculate the capacitance which is possible for a resistor R_Ω parallel to a CPE according to the formula:

$$C_{CPE} = (T * R^{1-P})^{1/P} \tag{27}$$

In Figure 14 an example of an impedance spectrum of a Ni/GDC fuel cell with two R-CPE elements with an ohmic resistance R_{Setup} is shown. The fitting curve is calculated iteratively to match the measurement points as good as possible. The ohmic resistance can be easily calculated through the subtraction of the high frequency x-axis intercept R_{Setup} from the low frequency intercept R_{total}. The two R-CPE elements are used to create two half circles. The left one represents the high frequency and the right the mid-range frequencies. The fitting then calculates quantitative results depending on the equivalent circuit diagram. [26] [8]

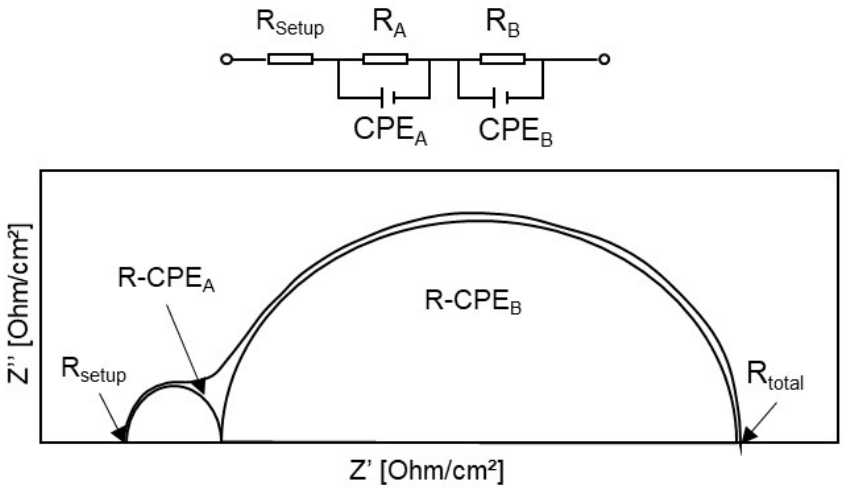

Figure 14: Equivalent circuit diagram for an SOFC which models electrode polarisation of two different electrode materials, electrolyte resistance and wire resistance. [26]

2.7.5 Pulsed laser deposition (PLD)

Pulsed laser deposition (PLD) is a physical vapour deposition technique that uses a high-powered pulsed laser to vaporise a material to precipitate it out of the gaseous state onto a sample. The sample as well as the target are placed in a vacuum chamber and the atmosphere can either be set to an ultra high vacuum there or be used to depose oxide thin films with the presence of a background gas like oxygen.

The laser pulse acts as an energy source like one in every physical vapour deposition method. With the absorption of the laser on the surface the energy is converted into an electronic excitation and further into thermal and mechanical energy which evaporates the target and forms a plasma on its surface. The vapour then expands in the vacuum, forms a cloud of high energetic species and travels to the heated substrate where it deposits. The properties of the thin film can be adjusted by variation of the substrate temperature, the oxygen partial pressure as well as the pulse rate. Under certain conditions the stoichiometry of the target can be changed on the way to the substrate. The principle of the device is shown in Figure 15. [36]

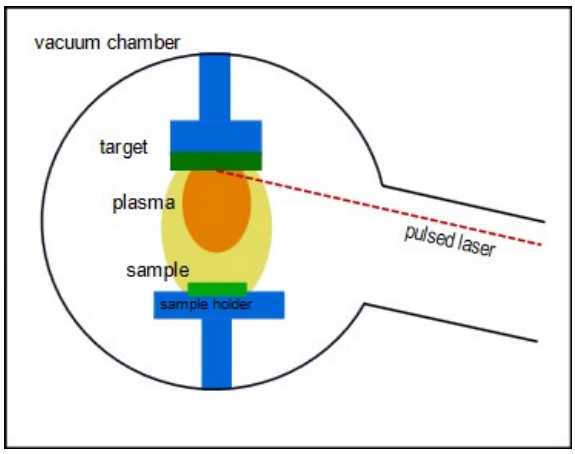

Figure 15: PLD chamber setup. The sample is fixed on a heated restraint. A pulsed laser is focused on the targed where a plasma forms which enables traveling of molecules, atoms and ions to the sample.

3 Experimental

3.1 List of used materials

Table 1: Used materials in the work

Material	Description
Photoresist	ma-N 1420 Negativ Photoresist (Micro Resist Technology GmbH, GER)
Developer	ma-D 533S Developer for Photoresis (Micro Resist Technology GmbH, GER)
YSZ100	ZrO2:Y (100)K (9.5 mol% Y2O3) single sided polished, single crystal, 10x10x0.5 mm (Crystec, GER)
YSZ-B	YSZ powder with PVA binder (Inframat, Advanced Materials)
GDC10	Treibacher Austria, $Ce_{0.9}Gd_{0.1}O_{1.95}$
GDC10 + Ni70	Heraeus Electronic Materials, Item: CL82-10336
NiO	Nickel(II)oxide nanopowder, $< 50nm$ 99.8%, Aldrich Lot: MKBX7741V
Ink-vehicle	ZrO2:Y (100)K (9.5 mol % Y2O3) single sided polished, single crystal, 10x10x0.5 mm (Crystec, GER)
Nitrogen gas	AirLiquide Nitrogen gas
Carbon dioxide gas	AirLiquide Carbon dioxide, ÖNORM EN ISO 14175-C1-C
1% O_2 gas	AirLiquide 1% Oxygen in 99% Nitrogen, UN 1956
2.5% H_2 gas	AirLiquide Arcal^{TM}10, ÖNORM EN ISO 14175-R1-ArH-2,4
Ethanol	Ethanol absolute 99.97%, VWR Chemicals, EC200-578-6

3.2 List of used devices

Table 2: Used Devices

Device	Description
PLD Laser	KrF (248 nm) excimer laser (Lambda COMPexPro 205F)
Pyrometer	Heitronics KT19.99
Uniaxial Press	KIP-PK Ø25 (Paul-Otto Weber Maschinen- und Apparatebau GmbH, GER)
Sintering Furnace	CWF1300 (Carbolite, GER)
Tube Furnace	Carbolite 1800, CTF18/–/300
Spincoater	Delta6RCTT (SUSS MicroTec, GER)
UV lamp	350W high pressure Hg lamp, maximum intensity 365nm (Ushio Inc., JAP)
Sputter machine	MED020 Coating system, QSG100 Quartz Film Thickness Monitor (BAL-TEC, now Leica Microsystems, AT)
EIS measurement device	Alpha-A High Performance Frequency Analyzer & Electrochemical Test Station POT/GAL 30V/2A (Novocontrol Technologies, GER)
Furnace (Micro-Macro setup)	Eurotherm 2000
Furnace (Macro setup)	Eurotherm 2000
MFC	Brooks instruments GF series, 200sccm & TYLAN FC280S, 200sccm & TYLAN FC260, 1000sccm
Thermolino	Temperature measurement device

3.3 MS calibration

For the required calibration of the mass spectrometer, different mixing ratios of carbon monoxide to carbon dioxide (0%, 20%, 50%, 100% CO) were induced into the test bench with the mass spectrometer connected. Every mixing ratio was measured until a steady signal was obtained. Due to the fact that the baseline of the MS signal of CO drifted over weeks and a recalibration was not possible to reiterate before each single measurement, the MS signals of the different ratios x_n were related on the baseline signal x_0 to get the quotient S_n.

$$S_n = \frac{x_n}{x_0} \tag{28}$$

Then the CO amounts were plotted over the belonging values S_n and were matched with a linear fitting ($R^2 = 0.9952$).

$$\omega_{CO} = 8.94 * S - 12.01 \tag{29}$$

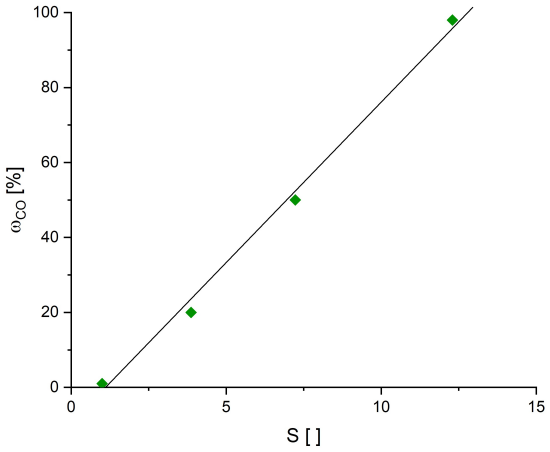

Figure 16: Calibration fit of CO on the mass spectrometer.

For the calculation of the CO amount during the measurement of the samples, the value S was calculated out of the MS results and matched with the received linear fitting (see equation 29).

3.4 Sample preparation for electrochemical impedance spectroscopy measurements

3.4.1 Micro-electrodes

One-sided polished single crystals of YSZ (100) were cleaned with ethanol in an ultrasonic bath to remove residues of dust and fat and dried with nitrogen gas afterwards to remove possible particles from the surface. On the unpolished side a porous electrode (Pt-YSZ) was applied. For that a paste of Pt-YSZ nanopowder mixed with inc vehicle was painted and sintered at $(1050°C, 3h)$. After another cleaning with ethanol, a layer of approximately $10nm$ of platinum was sputtered on the polished side. A lithographic mask was applied on the platinum layer. The substrate was cleaned with ethanol and dried with nitrogen. Afterwards a photoresist was applied on the surface with the aid of a spin coater. After drying a negative mask with the desired pattern of the power collectors was placed on top of it. With an UV lamp the uncovered spaces of the photoresist polymerised and hardened. With a developer unpolymerised residues of the photoresist were removed. Through ion beam etching the uncovered part of the platinum layer had been removed and only the desired pattern of platinum remains on the surface.
To prevent a permanent coating in the next step, the contact parts of the power collectors were covered with GDC paste. With Pulsed Laser Deposition (PLD), a $200nm$ layer of GDC has been applied as cathode at $600°C$ and $4 * 10^-5$ bar in O_2. In the ultrasonic bath in ethanol the protection layer of GDC paste was removed to reveal the complete electrolysis cell.

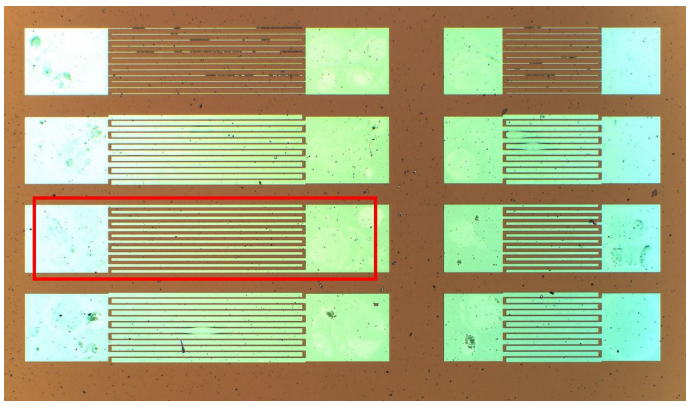

Figure 17: Mesh of micro-electrodes. The mesh is made of a platinum layer where the excess is etched away after a litographic application of the wanted mesh. The connecting parts (big squares) are then covered and an electrode is applied on the top. The sice of the big meshes is $0.7mm * 2mm$. For the measurement the mesh pointed out with a red square was used.

Beside pure GDC layers also GDC with nickel had to be measured at the micro-electrodes. Therefore a nickel oxide nano powder was diluted into the inc vehicle and pure ethanol (1:2) to get a approximately 1% solution.
This was then applied on the GDC electrode of a micro electrolysis cell with a spin coater. In the reducing atmosphere of the test bench, nickel oxide reduces to nickel, resulting in small nickel particles on the surface.

3.4.2 Macro-electrodes

For the preparation of the substrate, about $15g$ of Yttrium stabilized zirconium oxide nanopowder with binder was given into a press mould and was compressed with an uniaxial press with 2.5t for 300s into a 25mm cylindrical green body. Afterwards this was sintered at $1400°C$ for $3h$ and had a shrinkage of about 10%. To create the substrates, the suchlike formed cylinder has been sliced in wafers with a thickness of $0.4mm$ with a diamond cutting blade and was later on polished with a diamond polishing wheel.

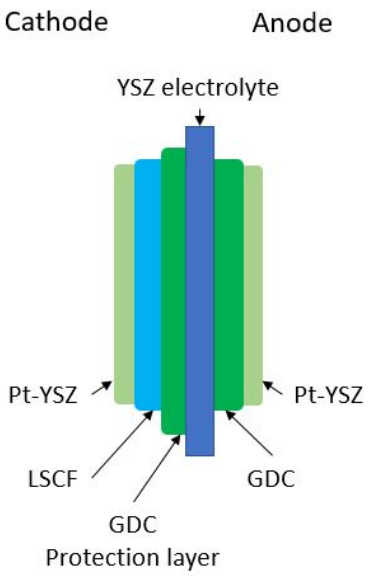

Figure 18: Schematic design of the used electrolyse cell. On the right side of the YSZ electrolyte is the cathode which is carried out with a GDC-electrode and a Pt-YSZ connector. The anode is made of a GDC protection layer, a LSCF-electrode and PT-YSZ-coating as connector.

Two different GDC pastes were prepared from GDC nano-powder and NiO nano-powder. The for the first, 1g of GDC nano-powder was mixed with 1g of ink-vehicle and 1ml of ethanol. For the second, to 0.9g of GDC nano-powder 0.1g NiO was added and mixed with 1g of ink vehicle and 1ml of ethanol. The two samples were mixed in a ball mill for 15 minutes and afterwards the ethanol was vaporised on a heating plate. The third GDC paste was a already finished paste with an amount of 70% of NiO inside with ink-vehicle.
The formed polycrystalline substrates were cleaned of dust and oil in an ultrasonic bath in pure ethanol. After drying with nitrogen gas the electrodes were applied. Through screen printing, a $10mm$ circle of each GDC paste (0% NiO, 10% NiO, 70%NiO) was printed onto substrates, dried at $130°C$ and a layer of Pt-YSZ as power collector was painted on and dried again. On the other side of the YSZ wafers a protection coat of GDC was applied.

The half electrode was sintered at $1150°C$ for $3h$ in an electrical furnace.

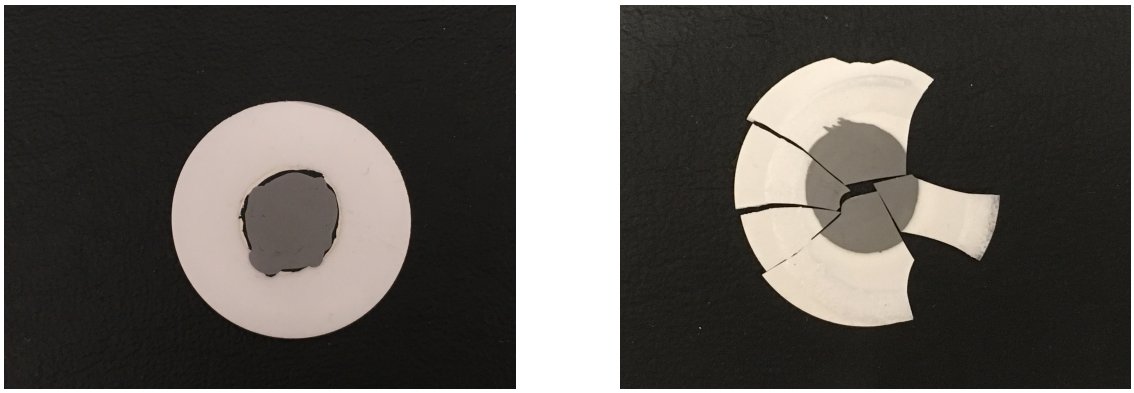

Figure 19: Finished SOFC cells before and after measurement. At the cooling process the electrode shattered due to the thermal tensions induced.

To finish the electrolysis cells, a layer of LSCF paste was painted on the protection coats and after drying at $130°C$ Pt-YSZ power collectors were applied on that side too. The second sinter process was performed at $1050°C$ for $3h$. Before implementing of the cell into the test bench, the resistances within the Pt-YSZ layers was measured to assure a percolating platinum layer.

The inner surface O of the GDC layer was calculated according to the Sauter diameter of the particles $(0.5\mu m)$, the porosity $\epsilon(0.4)$, the degree of fusion f (0.5) which reduces the particle surface through connection of particles, the diameter d $(1cm)$ and thickness of the sample h of the cell. First the whole volume V of the cell was calculated with:

$$V = \frac{d^2 * \pi}{4} \tag{30}$$

Then the porosity as well as the degree of fusion were taken in account to calculate the resulting inner surface:

$$O = \frac{6 * (1 - \epsilon)}{h} * V * (1 - f) \tag{31}$$

3.5 Measurement

3.5.1 Macro-electrodes

The electrolysis cells have been mounted on the alumina tube with a Duran glass sealing ring below and the GDC electrode facing into the inner gas chamber. During the heating as well as the whole measurement the outer gas room was fluently spilled with $50cm^3/min$ 1% O_2 in argon. The system was heated up to $700°C$ and the temperature was never reduced lower than that temperature during the measurement time. Measurements were taken at different temperatures and with different biases applied. In the beginning, for characterization, the inner gas chamber was filled with $50cm^3/min$ wet 2.5% H_2. The humidification was carried out with a chamber of water in the supply line at $22°C$ and atmospheric pressure.

Impedance spectra have been acquired at temperatures between $700°C$ and $850°C$ in $50°C$ steps and a bias interval from $0V$ to $1.6V$ in $0.2V$ steps. The same cycle was then made with a gas flow of $50cm^3/min$ CO_2. The same series of impedance spectra was retried after all measurements before cooling-down.

Subsequently current/voltage measurements were taken in $50cm^3/min$ CO_2. These have been taken at a furnance temperature of $850°C$ which led to an electrode temperature of about $800°$.

For the current/voltage measurements different voltage and current waveforms have been executed. In the beginning a linear increase of voltage up to $2V$ within $10min$ and back to $0V$ was measured. Then a voltage of $2V$ was applied for an hour to see signs of degradation of the SOEC. Measurement series with an increase of voltage up to $4V$ were carried out. To get a certain amount of carbon monoxide in the exhaust a current of $150mA$ was applied.

Each measurement was conducted with a mass spectrometer applied to measure the ingredients of the exhaust.

3.5.2 Micro-electrodes

Micro-electrodes have been placed with the counter-electrodes on the platinum sample holder and the micro-electrodes were connected with platinum needles at two current collectors of the mesh. The gas room was spilled with $50cm^3/min$ wet 2.5% H_2. The humidification was carried out with a chamber of water in the supply line at $22°C$ and

atmospheric pressure.

The furnace was heated up to $600°C$ and impedance spectra with a bias cycle from $0V$ to $1.6V$ with an interval of $0.2V$ steps was carried out for that temperature and up to $850°C$ in $50°C$ steps. Afterwards the gas flow was changed to dry $50cm^3/min$ CO_2. After an equilibration of the gas composition in the chamber the same measurement was reiterated. Current/voltage measurements were taken in CO_2 atmosphere. That proceeded at a furnace temperature of $850°C$. A linear increase of voltage up to $2V$ within $10min$ and back to $0V$ was scaled. The same measurement was done in 2.5% H_2. Additionally the test bench was cooled down and the whole measurement was retaken on another micro-electrode on the same sample. The mass spectrometer was not connected for this measurements because of the low cell surface and resulting low production rate of carbon monoxide.

4 Results and discussion

4.1 Film thickness

For the calculation of the efficiency of the cells, the inner surface has to be calculated. Therefore the thickness of the porous GDC layer has to be measured. To do that, the cross sections of the electrodes, which were broken before, were analysed with an optical microscope. As can be seen in Figure 20, the film thickness could be determined. The sample with just GDC had an average thickness of $6.94\mu m$, GDC with 10% nickel $4.63\mu m$ and the sample with 70% nickel had $4.77\mu m$. While the first two samples had a steady junction, an ablation of the platinum layer and also of parts of the electrode was observed. That might have happened during the cooling-down of the electrode in the course of the measurement, or potentially before, which could have affected the results.

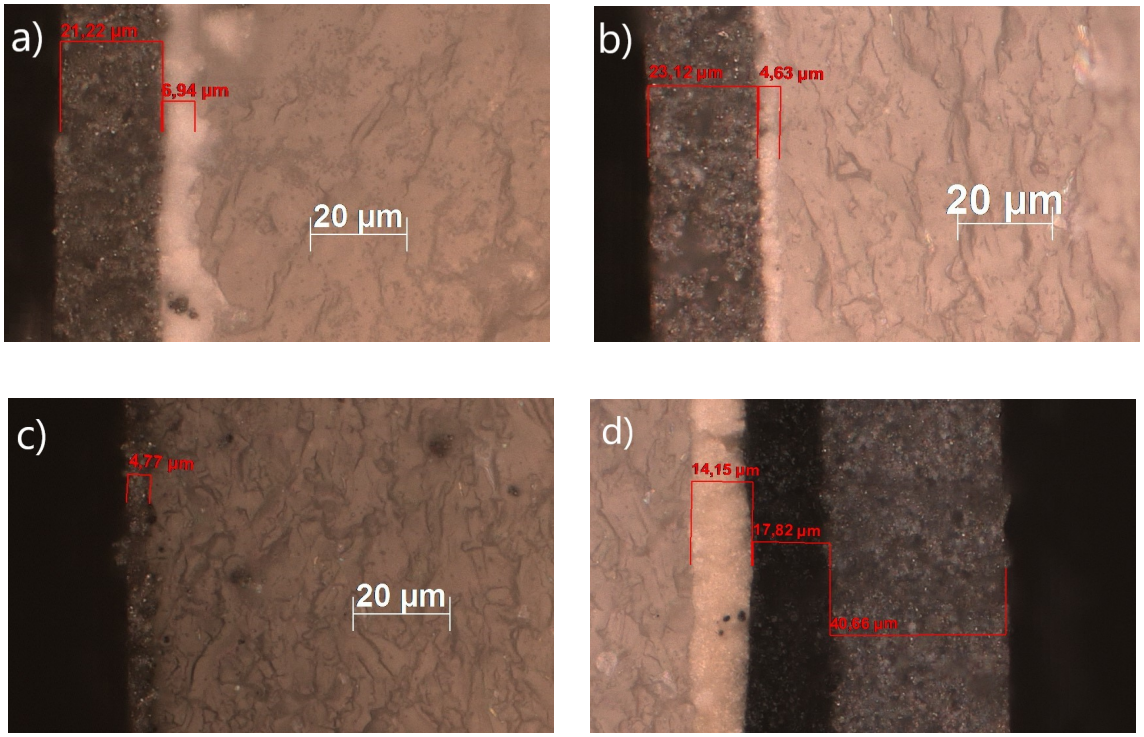

Figure 20: Cross section of the catode which is made out of GDC with platinum as connector. a) Electrode with GDC has an average thickness of $6.94\mu m$; b) GDC with 10% Ni with an average thickness of $4.63\mu m$; c) GDC with 70% of Ni has an average thickness of $4.77\mu m$ but the Pt layer is detached and parts of the GDC+Ni layer also broke during the measurement; d) The anode is made of GDC separating layer, a LSCF electrode and platium layer as connector.

4.2 Impedance spectroscopy

Impedance spectra were recorded to obtain the electrochemical surface polarisation resistance of the GDC electrodes with different amounts of nickel. The recorded data was plotted in a Nyquist plot to obtain the polarisation resistance as well as the resistance of the cables and set-up.

To be able to fit the data, an equivalent circuit diagram which is shown in Figure 21 was chosen for the fitting. The use of two serial connected resistances R parallel connected with CPE elements Q made it possible to obtain the polarisation resistance of the cell as well as the polarisation resistances for the GDC electrode. While the $R_{Cathodic}/Q_{Cathodic}$ element was for the micro-electrodes the polarisation resistance of PtYSZ, the porous electrodes had LSCF as counter electrode which has a more similar frequency spectra to GDC and a differentiation between them was harder to obtain.

$$R_{electr.pol.} = R_{PtYSZ} + R_{GDC} \tag{32}$$

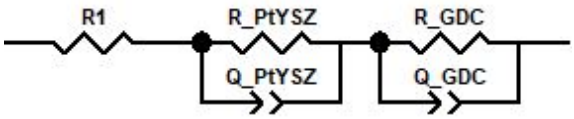

Figure 21: Equivalent circuit diagram used for the fitting of the impedance data.

Impedance spectra of porous electrodes were recorded in the beginning as well as in the end of the measurement to obtain information about the cell behaviour and processes which are responsible for polarisation over the course of time.

For micro-electrodes this was not possible because of frequent disconnections during the measurements due to the small current collectors and the improvised measurement set-up which is primarily for symmetrical cells. These disconnections required cooling-downs which made long measurement times required for multiple measurements complicated.

For the categorisation of the efficiency of the electrode material in the first place, impedance spectra of GDC micro-electrodes with a defined active surface of $1.4mm^2$ on YSZ single crystals (100) with LSCF counter electrodes were taken and the results were plotted in a Nyquist plot (see Figure 22). The Nyquist plot didn't show perfect semicircles due to the different electrode materials with overlapping frequency spectra but with the equivalent circuit diagram (Figure 21), the two formed semicircles were fitted and thus, the resistances an capacities of the electrodes could be obtained.

The interesting outcome was that the cell with nickel applied had about half of the polarisation resistance of the clean GDC layer.

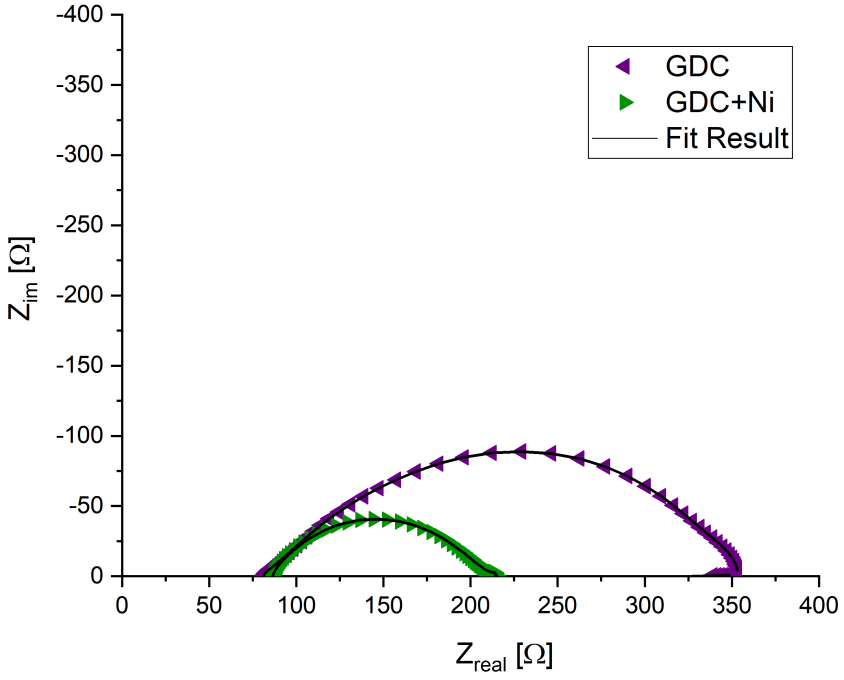

Figure 22: Measurement of GDC micoro-electrodes (cell sice is $1.4mm^2$) in CO_2 at $800°C$.

As well as for the micro-electrodes, the impedance spectra of porous electrodes in CO_2 have been measured and are shown in Figure 23. GDC with 10% nickel shows by far the lowest electrode polarisation resistance. The polarisation resistance of the 70% nickel sample happened to be extraordinarily high and had a deviation at the high frequency part which is not visible at the other electrodes. That could have been due to a low electronic or ionic conductivity or partly ablation of the Ni/GDC electrode. The other electrodes showed principally the same picture as the micro-electrodes, however with lower polarisation resistances.

The impedance spectra of all samples are shown in Table 3.

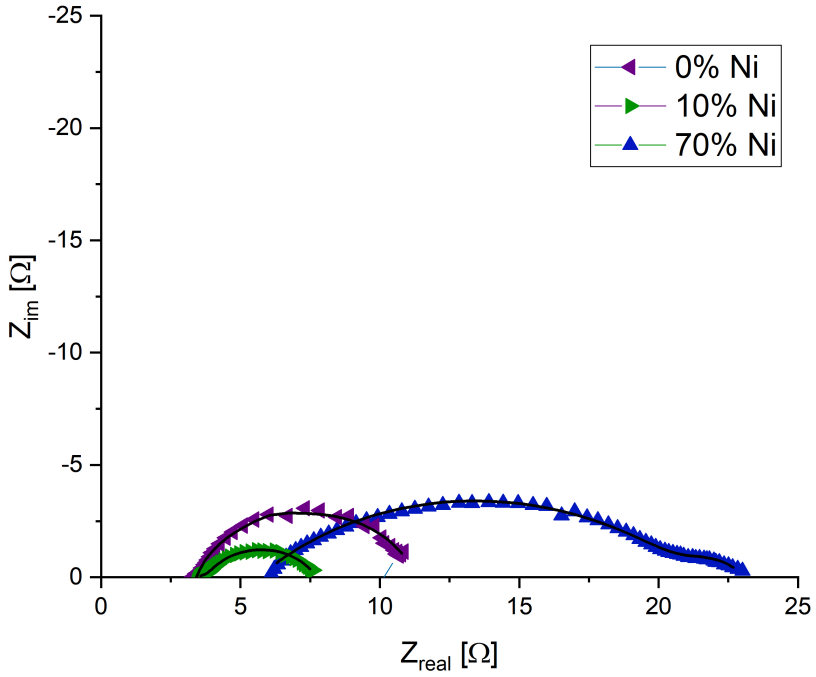

Figure 23: Comparison of the impedance spectra of working electrodes with different amounts of nickel in CO_2 at $800°C$.

The collected polarisation resistances of the impedance spectra are stated in Table 3. The resistances as well as the capacities of the micro-electrodes are far higher than those of porous electrodes which was expected due to the difference in size.

The P factor which displays the approximation of a CPE element to the real capacitance occurred to be over 0.7 for all but one sample, which makes it possible to accept the values as the real capacitances. For the 70% nickel sample the P factor was below 0.7 which states that other constituents than only a capacitance had been obtained and the result is not reliable. The doping of nickel principally made the fit imperfect through adding other elements which could not be fitted with the used equivalent circuit diagram. At the micro- and macro-electrodes the polarisation resistances dropped through doping with nickel. The capacitance shows the change of oxygen-stoichiometry with the over-voltage and is dependent of the volume of the measured sample. The difference of the volumes between the micro- and macro-electrodes was about 10^4 which resembles that of the capacitance and let us assume that the whole electrode thickness was electrochemical active. Differences in the values could have been due to differences in thickness and also a deviation of the electrode build up, because the over-voltage on the cathode as well as on the electrolyte was different due to their sizes.

Table 3: Polarisation resistances at a gas flow of $50cm^3/min$ CO_2 and a bias of $1V$

Sample	**Polarisation resistance [Ω]**	**Cathodic polarisation resistance [Ω]**	**Cathodic capacity [C]**	**P factor []**
GDC micro-electrode	275.23	192.7	$5.93 * 10^{-6}$	0.82
GDC+10%Ni micro-electrode	129.54	114.9	$4.95 * 10^{-7}$	0.76
GDC macro-electrode	7.70	7.39	$4.97 * 10^{-2}$	0.91
GDC+10%Ni macro-electrode	6.27	5.90	$6.48 * 10^{-2}$	0.73
GDC+70%Ni macro-electrode	18.13	15.92	$3.39 * 10^{-1}$	0.54

Current/Voltage curves of the porous electrodes are compared to see a direct difference in their behaviour.

The current was hereby correlated to the geometrical surface of the sample. The voltage was reduced by the over-voltage of the electrolyte. Until about $0.6V$ the current stayed stationary at about $0A$ and raised afterwards linearly with the increasing voltage, which showed the start of the CO_2 electrolyse, which needs a certain over-voltage of about $0.7V$, which is also the open circuit voltage of the CO/CO_2 electrolysis reaction. The measurement results behaved according to their polarisation resistances. The doping of nickel increased the current per voltage but dropped because of an increase to 70% nickel. Further was no current limitation visible in the electrolysis until the maximum $2V$.

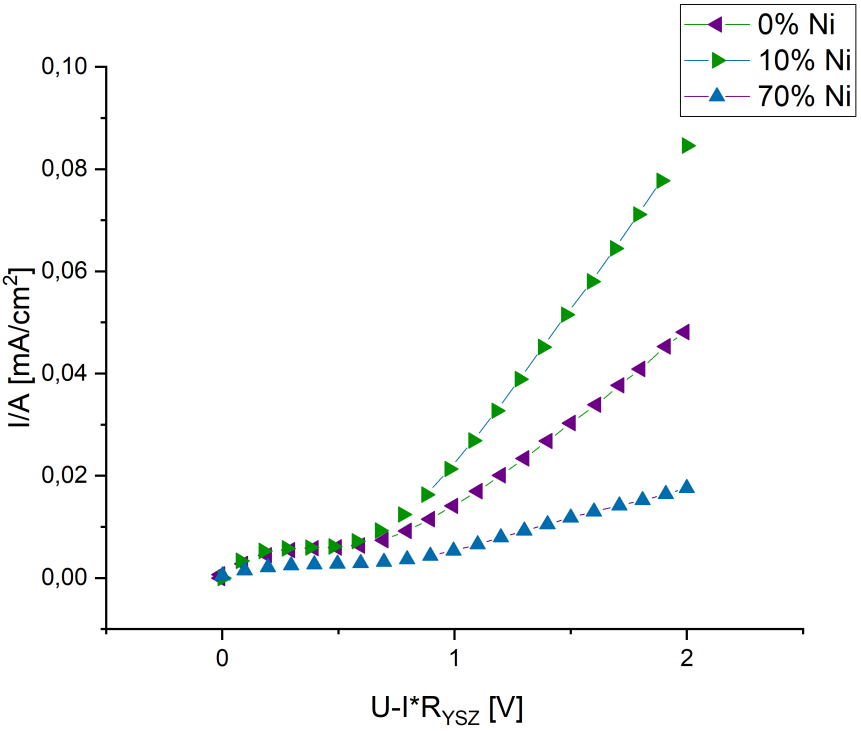

Figure 24: Current/Voltage curves on porous electrodes in CO_2 at $850°$.

4.3 Temperature influence

The influence of the temperature on impedance spectra was also measured and the results of that measurement is shown in Figure 25. While the temperature increased, the conductivity rose as well as the electrode kinetics. While the temperature rose linearly from one measurement to the next one, the polarisation resistance did not not follow a linear decrease but a logarithmic one. Also the resistance of the wires and the interface $R1$ to the electrodes decreased through this process. That leads to the assumption that the main part of the resistance $R1$ comes from the interface itself and not from the wires, because their resistance would increase due to their negative temperature coefficient of resistance.

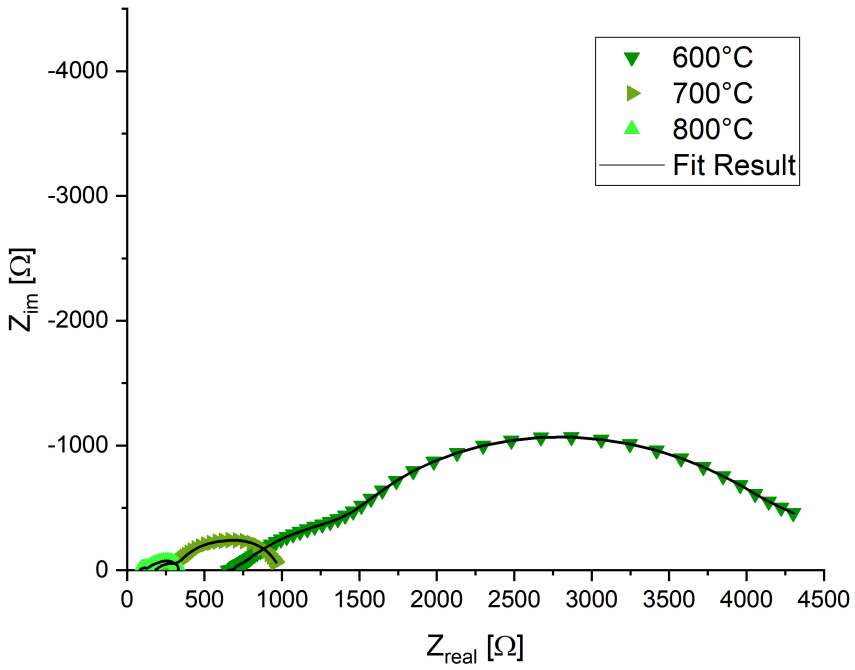

Figure 25: Influence of temperature on impedance spectra of GDC micro-electrodes with nickel partickles in CO_2.

To take a closer look at the influence of the temperature, Arrhenius plots of the electrolyse cells were prepared. At a Arrhenius plot the logarithmic values of a measurement are stated over the inverse of the temperature. The slope of the resulting curve states hereby the activation energy of the reaction.

The two measurements were the first ones to be carried out after heating (first the mea-

surement in H_2/H_2O and then in CO_2). Graphs for the results of porous cells in H_2/H_2O without bias applied and CO_2 with a bias of $1V$ (Figure 26 and 27) had been created. For the comparison of the activation energies the values are stated in table 4. The sample with 10% nickel had hereby the lowest activation energy at both measurement set-ups. An interesting part is the huge increase of activation energy for the 70% Ni sample. This could be due to a partial ablation of the cathode due to formation of carbon below the platinum layer in CO_2 atmosphere which would explain high resistances of this electrode at further measurements.

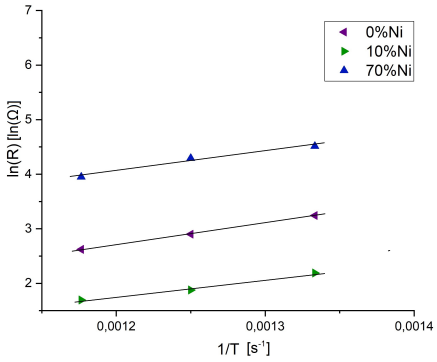

Figure 26: Arrhenius plots for electrolysis cells with different amounts of nickel in H_2/H_2O without bias applied in the beginning of the measurement time. The activation energy of the 0% nickel sample is $3960.9 J/mol$, for the 10% nickel sample $3168.3 J/mol$ and for the 70% nickel sample $3584.3 J/mol$

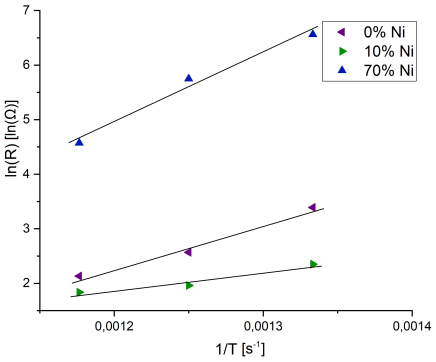

Figure 27: Arrhenius plots for electrolysis cells with different amounts of nickel in CO_2 at a bias of 1V in the beginning of the measurement time. The activation energy of the 0% nickel sample is $8050.5 J/mol$, for the 10% nickel sample $3315.2 J/mol$ and for the 70% nickel sample $12604 J/mol$

Table 4: Activation energy of porous macro-cells calculated from Arrhenius plots.

Sample	**Activation energy in H_2/H_2O at a bias of 1V [J/mol]**	**Activation energy in CO_2 at a bias of 1V [J/mol]**
GDC	3960.9	8050.5
GDC+10%Ni	3168.3	3315.2
GDC+70%Ni	3584.3	12604

4.4 Mass spectrometry

The ability to reduce carbon dioxide into carbon monoxide is the major part of the work and has to be measured. That was done through some different measurement set-ups. The first one was done applying $2V$ over a period of 1000s with a CO_2 flow of $50cm^3/min$. The current was measured as well as the amount of carbon monoxide in the exhaust. GDC with 10% nickel had hereby the best results in reduction of carbon dioxide just as in case of efficiency which is calculated as Faraday's efficiency where it has a rate of 88%. An interesting part of the carbon monoxide production measurement was the fact that the amount of it raised for all electrodes except the 10% nickel cell immediately. For that cell a jump occurred in the beginning and then it fell again before rising to its maximum. That leads to the assumption that carbon may have formed on the electrode due to the spontaneous start of the reduction and converted back with the electrolysis time through the Boudouard reaction. The efficiencies of all set-ups are presented in Table 5.

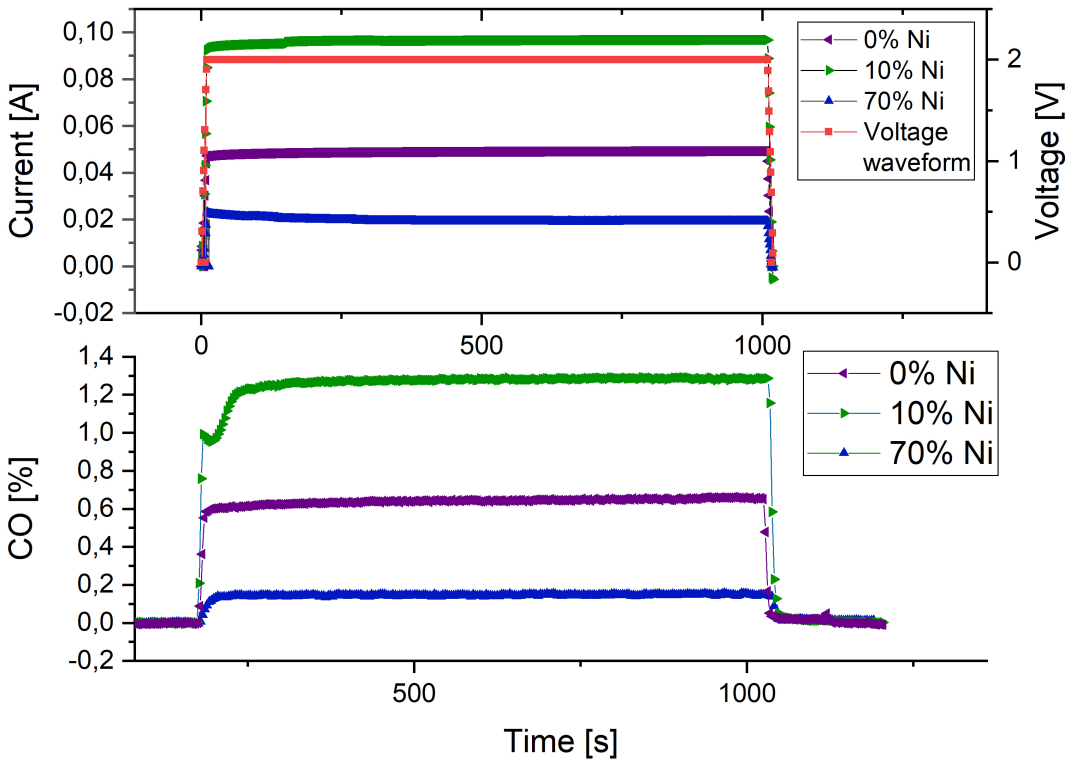

Figure 28: Curent over time at a stationary voltage of 2V with $800°C$ at $50cm^3/min$ CO_2 for cells with different porous electrodes. Carbon monoxide production rate during 2V applied with a CO_2 flow of $800°C$.

For the second set-up the voltage has been raised linearly to two volts and back to zero. The outcome for the electrodes were practically the same as before. The only difference was a higher, almost perfect efficiency for the 10% nickel electrode and a lower one for the 70% nickel electrode at the pinnacle of the measurement. The difference in the efficiency between the last measurement and this one could have occurred, because no carbon was able to form on the electrode due to the low measurement time and slow increase of voltage.

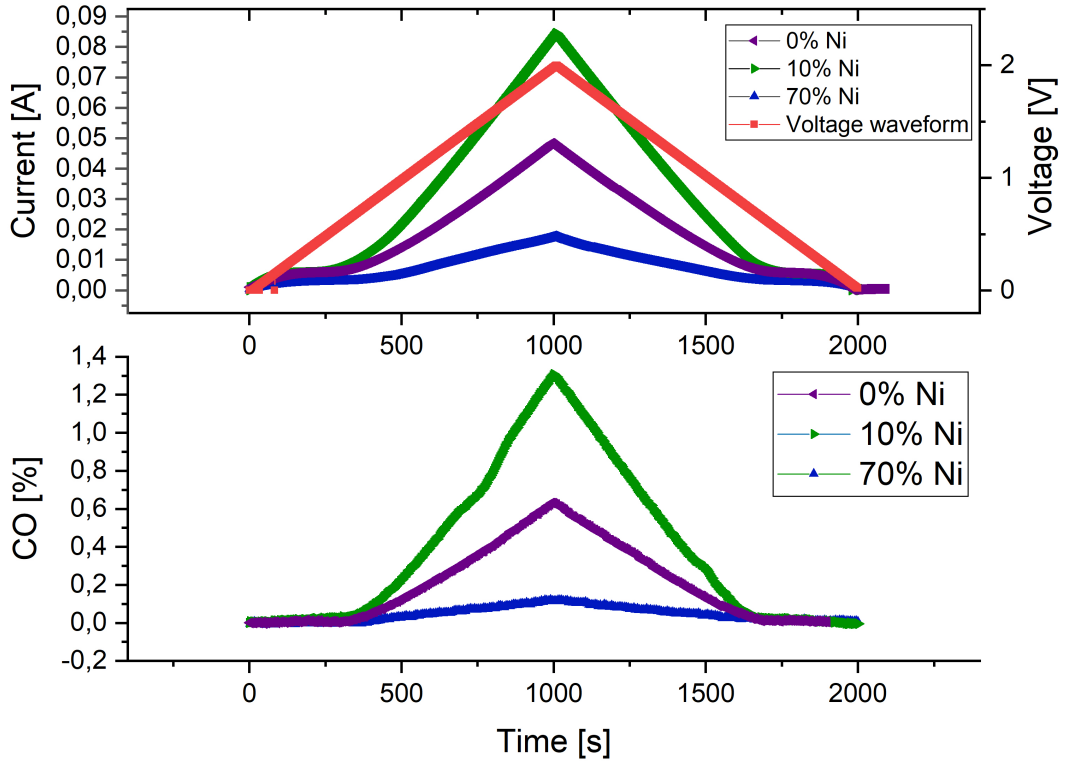

Figure 29: Current over time at a rising voltage from 0V to 2V and falling to 0V, measured for cells with different porous electrodes. That measurement was done at a temperature of $800°$C with a gas flow of $50cm^3/min$ CO_2. Carbon monoxide production rate during the rise of the voltage up to 2V with a CO_2 flow of $800°$C.

The third set-up was a stepwise increase of voltage to four volts to observe how much the cell is able to withstand and to see if a higher voltage has a negative impact on the sample. As witnessed, the efficiency of the cell did not drop and the amount of carbon monoxide rose linearly. Again at the raise from one to two volts at the 10% nickel sample the carbon monoxide production showed the same characteristic of not immediately rising to its maximum as before but didn't reproduce this at the other steps. The linear current increase showed furthermore that there was no gas diffusion limitation present.
At the 70% nickel sample was a far higher increase of current at the step to $4V$ visible than at the other increases but the CO_2 flow responded not the same way which seemed to cause more carbon production on the electrode.

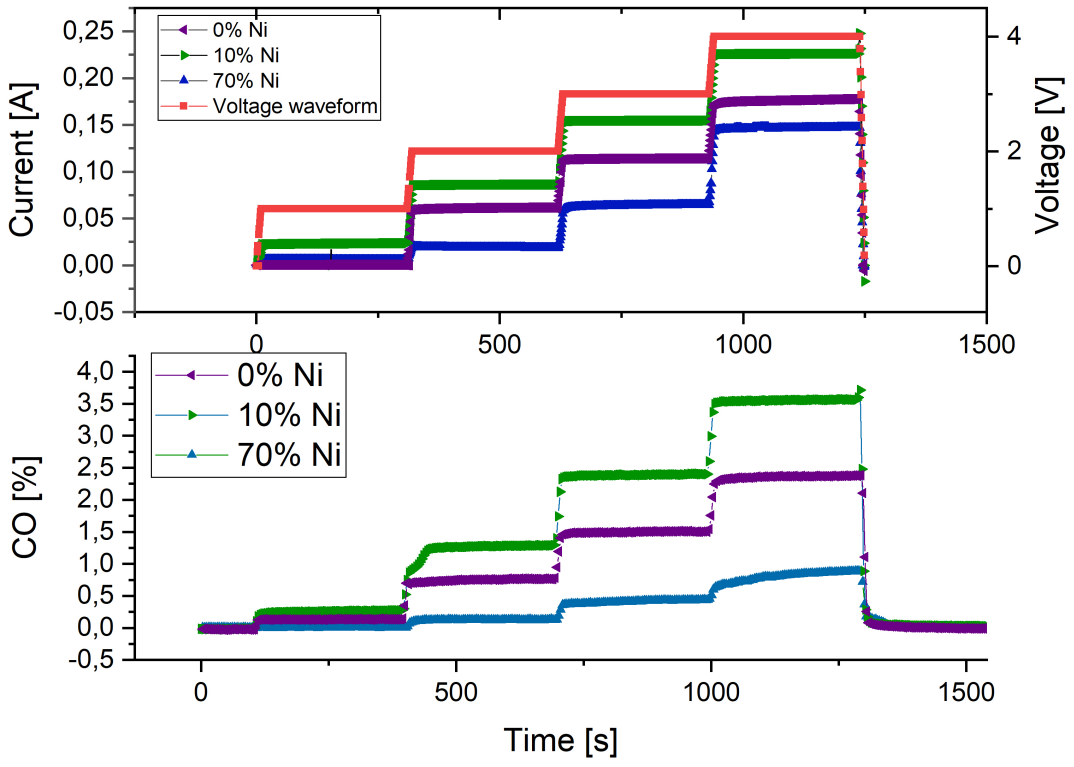

Figure 30: Stepwise increas of voltage up to 4V, measured for cells with different porous electrodes. Voltage waveform is stated in red. That measurement was done at a temperature of $800°$C with a gas flow of $50cm^3/min$ CO_2. Carbon monoxide production rate during the stepwise increase of voltage up to 4V. That measurement was done at a temperature of $800°$C with a gas flow of $50cm^3/min$ CO_2.

The last set-up was used for a carboxylation reaction set-up, in collaboration with the Institute of Applied Synthetic Chemistry, where an amount of at least 4% carbon monoxide in the exhaust was required. Therefore the current was set to $150mA$ to create at least 2% in $50cm^3/min$ or 4% in $25cm^3/min$ which was possible due to a linear distribution because diffusion limitations did not seem to happen at low concentrations of CO. Lower gas flows were not possible to be measured because of the limitations of the mass flow controllers. The amounts of CO in the exhaust at $25cm^3/min$ were 4.6% for the 10% nickel sample and 4.2% for pure GDC. To reach the goal the 10% nickel sample needed the lowest voltage and the undoped sample needed more than twice the voltage. The cell with the highest amount of nickel was not able to reach the carbon monoxide amount and it seems like it has used up the applied energy to create heat or not observed side reactions.

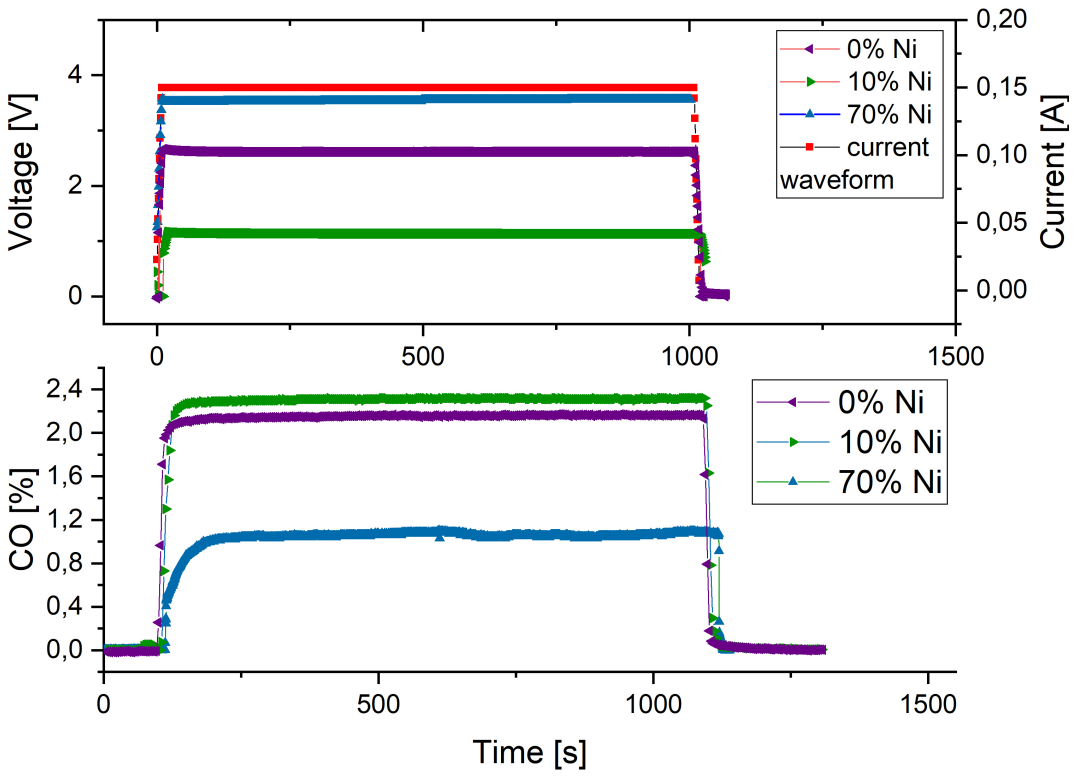

Figure 31: Voltage at a stable current of 150mA over 1000s, measured for cells with different porous electrodes. That measurement was carried out at a temperature of $800°$C with a gas flow of $50cm^3/min$ CO_2.

Some of the results of the efficiency calculation were slightly higher than 100%. That may have occurred due to the fact that the gas flows, the amount of carbon monoxide

created and the current applied, have a variance from the real values which may lead to a deviation of the results. Also the pressure during the measurement was primarily athmospheric pressure ($1.013bar$) but varied due to not perfect conditions in the laboratory and may have influenced the calculation. All that taken in account, the results should not have a standard variation of more than 4%. The efficiencies show a distinct picture of the applicability of the different cells as well as the fact that an over-endowment of nickel caused more negative than positive effects in CO_2 electrolysis.

Table 5: Efficiencies of CO_2 electrolysis in different measurement set-ups at different porous electrodes.

Material	**Faraday efficiency**
2V stationary:	
GDC	86%
GDC+10% Ni	88%
GDC+70% Ni	51%
triangle to 2V:	
GDC	85%
GDC+10% Ni	101%
GDC+70% Ni	43%
steps 3V:	
GDC	87%
GDC+10% Ni	102%
GDC+70% Ni	44%
steps 4V:	
GDC	89%
GDC+10% Ni	103%
GDC+70% Ni	39%
150mA stationary:	
GDC	95%
GDC+10% Ni	102%
GDC+70% Ni	47%

4.5 Degradation

In the beginning of the measurements and before cooling, impedance spectra have been obtained to conclude on the degradation of the samples over the course of time. The measuring time was only one week at all and for real application a test over more then $40000h$ will be necessary for the usage as a stationary device. Although a definite degradation of all cells was visible in course of one week, a further fast degradation is not inevitably going to happen for the samples without and with small amounts of nickel.
For the 70% nickel sample the polarisation resistance increased over 600%. Compared with the measurements done the use of it in CO_2 atmosphere seems not possible. The polarisation resistances for that conclusion are labelled in Table 6.

Table 6: Polarisation resistance differences of cells with electrodes having different amounts of nickel over the measurement time of one week. Polarisation resistances are mesured in CO_2 at a voltage of $1V$

Material	**Polarisation resistance in the beginning [Ω]**	**Polarisation resistance at the end [Ω]**
GDC	7.70	11.90
GDC+10% Ni	6.33	8.41
GDC+70% Ni	18.13	113.66

4.6 Comparison of thin film vs. porous electrodes

To compare all samples, the obtained data is now referred on the possible active surface of the samples as well as on their geometrical surface. Therefore a porosity of 40% and a degree of fusion of 50% was assumed for the porous samples.
The values for the micro-electrodes were above $283 mA/cm^2$ while the values of the porous electrodes are between $0.7 mA/cm^2$ and $3.7 mA/cm^2$. The exact values are given in Table 7.

Table 7: Measured current is referred on the active surface of the sample at a voltage of $2V$. The current is referred onto the calculated inner surface of the electrodes (macro-electrodes: $28.27 cm^2$; micro-electrodes $1.4 mm^2$) and to the geometrical surface (macro-electrodes: $0.79 cm^2$; micro-electrodes $1.4 mm^2$)

Material	**Current per inner surface [mA/cm^2]**	**Current per geometric area [mA/cm^2]**
GDC macro-electrode	2.90	62.39
GDC+10% Ni macro-electrode	5.70	123.11
GDC+70% Ni macro-electrode	1.12	24.19
GDC micro-electrode	283.5	283.5
GDC+Ni micro-electrode	370.3	370.3

The huge gap between the porous and the thin film electrodes suggests that not the whole surface area of the porous electrode was used for CO_2 reduction. This could be due to a gas diffusion problem towards the reducing part of the electrode, a limitation of the electronic or ionic conductivity in the cathode or because of an electrode poisoning. A diffusion would lead to a limiting current, but concerning the fact that the cells were able to be tested up to $4V$ and the current was not limited a gas diffusion limitation is rather unlikely. The limitation of the ionic or electronic conductivity would be visible in the capacitances of the cathodes. But the capacitances between thin film and porous electrodes have a huge difference (see Table 3) and this leads to the third possible reason of an electrode poisoning. The sealing of the electrode is made of Duran glas which could partly diffuse onto the electrodes at high temperatures leading to a coverage and reducing the available surface. The fact that even the geometrical surface of the micro-cells had far superior results could be on account of impurities in the porous samples, investigated

in a two channel mode. It is less likely for the PVD prepared cells investigated in a single channel mode.

Another point of a possible mistake lies in the calculation of the inner surface of the porous electrodes. The size of the particles is between $2.5\mu m$ and $1.1\mu m$ (see Figure 32) due to agglomeration in the sintering process. For the calculation a Sauter mean diameter of $0.5\mu m$ was chosen. But at an increase of the particle diameter concerning higher agglomeration rates during the sintering the inner surface would be far less.

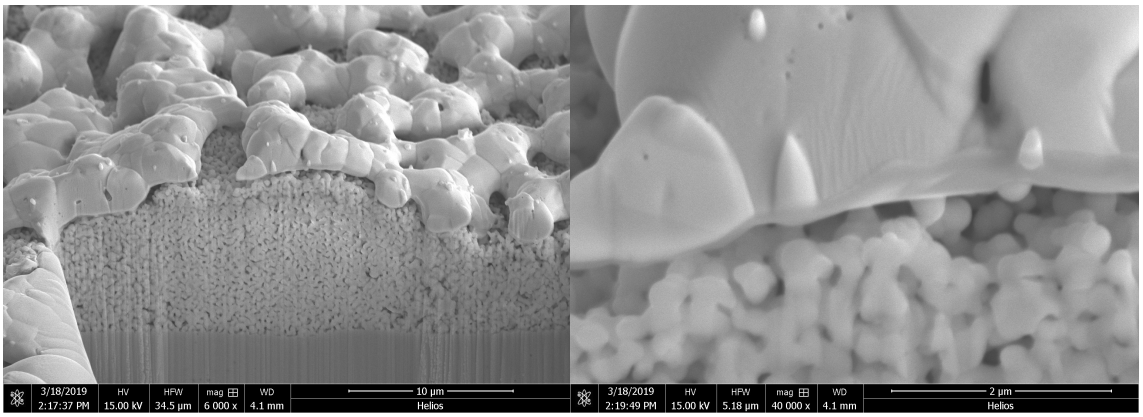

Figure 32: SEM image of a focused ion beam milled cross-section of the GDC+10%NiO layer on polycrystalline YSZ. Large particles on the surface are from the Pt paste current collector. Provided by Courtesy of Tobias Huber and Kyushu University

5 Conclusion

Two types of solid oxide cells were successfully fabricated, obe with a morous GDC electrode and one with a GDC thin film electrode. The colls with porous electrodes could be used to produce carbon monoxide out of carbon dioxide. Faradaic efficiencies in the range of 39% to 103% were obtained. Every cell was measured over a whole measurement time of a week and impedance spectra were taken in the beginning and the end to observe major changes in their performances. Only moderate degradation took place though for real stationary application a measurement time over more than $40000h$ would be required. The currents at 2V cell voltage were referred to the surface area of the electrodes. Surprisingly the thin film electrodes were far superior to the porous samples with nominally almost two orders of magnitude larger current densities. It seems that not the whole inner surface of the porous samples was active due to an electrode poisoning. The introduction of nickel increased the conductivity in the cells and lowered the cell resistance. The best results in terms of CO_2-reduction as well as cell efficiency was achieved for a "doping" of the GDC-electrodes with 10% nickel. 70% nickel however, lead to delamination of the electrodes during the measurement. Interestingly, GDC-cells without percolating nickel have still sufficient electrical conductivity for an application in electrolysis cells. For a subsequent carboxylation reaction an amount of at least 4% carbon monoxide had to be created over half an hour. This turned out to be possible: At a current of $150mA$ and a flow rate of $25cm^3/min$ CO_2 an amount of 4.6% was produced, which made it possible.

6 Appendix

6.1 Glossary

A	Area [m^2]
C	Capacitance [F]
$\dot{V}_{CO}$	CO flow rate [m^3/s]
$\dot{V}_{CO_2}$	CO_2 flow rate [m^3/s]
D	Diffusion coefficient [mol/L]
d	Thickness of the thin film [m]
e	Elementary charge [C]
ΔG	Free enthalpy change [J/mol]
ΔH	Enthalpy change [J/mol]
ΔS	Entropy change [J/mol*K]
E_A	Activation energy [eV]
F	Faraday constant [C/mol]
f	Geometry factor []
f	Frequency [1/t]
I	Electrical current [A]
I_{theor}	Theoretical current [A]
i(t)	Alternating current [A]
i_0	Alternating current amplitude [A]
k_B	Boltzmann constant [eV/K]
N_A	Avogadro constant [1/mol]
p	Atmospheric pressure [Pa]
Q	Charge [C]
R	Universal Gas constant [J/mol*K]
T	Temperature [K]
τ	Frequency dependent time constant [$1/\Omega$]
U	Voltage [V]
U_e	Open circuit voltage [V]
u(t)	Alternating current [V]
u_0	Alternating current amplitude [V]

v	Speed [m/s]
W_{chem}	Chemical work [J/mol]
W_{el}	Electrical work [J/mol]
ω	Frequency [Hz]
ω_{CO}	Amount of CO [%]
x_n	MS signal []
x_0	MS baseline signal []
z	Valency []
Z	Impedance [Ω]

6.2 Acronyms

CO	Carbon monoxide
CO_2	Carbon dioxide
CPE	Constant phase element
DMFC	Direct methanol fuel cell
EIS	Electrochemical impedance spectroscopy
GDC	Gadolinium doped ceria
LSCM	$(La,Sr)(Cr,Mn)O_{3-\delta}$
MIEC	Mixed ionic and electronic conductor
MFC	Mass flow controller
O_2	Oxygen
PEMFC	Polymer electrolyte membrane fuel cell
SOEC	Solid oxide electrolysis cell
SOFC	Solid oxide fuel cell
TPB	Triple phase boundary
YSZ	Yttria stabilized zirconia

List of Figures

List of Tables

References

[1] *http://photonicswiki.org/index.php?title=Perovskites. 28.08.2019*.

[2] https://de.wikibooks.org/wiki/tabellensammlung_chemie/_thermodynamische_daten. 2019-10-30.

[3] https://de.wikipedia.org/wiki/fluorit. 2019.09.04.

[4] Weber A. *Entwicklung von Kathodenstrukturen für die Hochtemperaturbrennstoffzelle SOFC*. Universität Fridericiana Karlsruhe. 2002. p. 53 - 56.

[5] Nenning Andreas, Volgger Lukas, Miller Elizabeth, Mogni Liliana V., Barnett Scott, and Fleig Jürgen. *The Electrochemical Properties of Sr(Ti,Fe)$O_{3-\delta}$ for Anodes in Solid Oxide Fuel Cells*, volume 164 of *Journal of the Electrochimical Society. 2017*. p. 364 - 371.

[6] Bauen Ausilio. *Future energy sources and systems-Acting on climate change and energy security*, volume 152 of *Journal of Power Sources. 2006*. p. 893 - 901.

[7] Hans Dieter Baehr and Stephan Kabelac. *Thermodynamik: Grundlagen und technische Anwendungen*. Springer-Lehrbuch. 2009. 14 edition. page 348 - 351.

[8] Evgenij Barsoukov and James Ross Macdonald. *Impedance spectroscopy*. WILEY-VCH. 2018. 3 edition. p. 1 - 38.

[9] Herbert Budzikiewicz and Mathias Schaefer. *Massenspektrometrie*. WILEY-VCH. 2012. 6 edition. p. 10 - 45.

[10] Steven J F Byrnes. *Basic theory and phenomenology of polarons*. Department of Physics, University of California at Berkley. 2008.

[11] C.B. Carter and M.G. Norton. *Ceramic materials: Science and engineering*. Springer. 2007. 2 edition. p. 187 - 203.

[12] Barsoukov E. and Macdonald J.R. *Impedance Spectroscopy: Theory, Experiments and Appilcations*. Wiley-Interscience. 2005. p. 6 - 12; 346 - 355; 469 - 475.

[13] Zhuoluo A. Feng, Farid El Gabaly, Xiaofei Ye, Zhi-Xun Shen, and William C. Chueh. *Fast vacancy-mediated oxygen ion incorporation across the ceria–gas electrochemical interface*, volume 5 of *Nature Communications. 2014*. p. 1 - 7.

[14] Strong Frederick. *Faraday's laws in one equation*, volume 38 of *Journal of Chemical Education. 1961*. p. 98.

[15] Qingxi Fu, Corentin Mabilat, Mohsine Zahid, Annabelle Brisse, and Ludmila Gautier. *Syngas production via high-temperature steam/CO_2 co-electrolysis: an economic assessment*, volume 3 of *Energy & Environmental Science. 2010*. p. 1382.

[16] Ludwig J. Gauckler. *Funktionskeramik*. ETH Zurich. 2001. p. 128 - 170.

[17] Zhu H., Ricote S., Coors S.G., Chatzichristodoulou C., and Kee R.J. *Equilibrium and transient conductivity for gadolium-doped ceria under large perturbations: II. Modeling.*, volume 268 of *Solid State Ionics. 2014*. p. 198 - 207.

[18] Carl Hamann and Wolf Vielstich. *Elektrochemie*. WILEY-VCH. 1998. 3 edition. p. 9 - 53.

[19] Salmang Hermann and Scholze Horst. *Keramik*. Springer Schience & Business Media. 2006, 7 edition. p. 2 - 6.

[20] Koettgen J. and Grieshammer S. *Understanding the ionic conductivity maximum in doped ceria: Trapping and blocking.*, volume 21 of *Physical Chemistry Chemical Physics. 2018*. p. 14291 - 14321.

[21] Maier Joachim. *Physical Chemistry of Ionic Materials Ions and Electrons in Solids*. John Wiley&Sons. 2004. 1 edition. p. 14 - 20.

[22] Mats Johnsson and Peter Lemmens. *Crystallography and Chemistry of Perovskites*. John Wiley & Sons, Ltd. 2007.

[23] Irvine J.T.S. *The bourner lecture: Power sources and the new energy economy*, volume 136 of *Journal of Power Sources. 2004*. p. 203 - 207.

[24] Cassidy M., Lindsay G., and Kendal K. *The reduction of nickelzirconia cermet anodes and the effects on supported thin electrolytes*, volume 61 of *Journal of Power Sources. 1996*. p. 189 - 192.

[25] Mogensen M., Sammes N.M., and Tompsett G. A. *Physical, chemical and electrochemical properties of pure and doped ceria.*, volume 129 of *Solid State Ionics. 2000*. p. 63 - 94.

[26] Orazem M.E. and Tribollet B. *Electrochemical Impedance Spectroscopy*. Wiley. 2008. p. 363 - 370; 421 - 429.

[27] Nguyen Q. Minh. *Ceramic Fuel Cells*, volume 76 of *Journal of the American Ceramic Society. 1993*. p. 563 - 588.

[28] Q. Minh Nguyen. *Solid oxide fuel cell technology - features and applications*, volume 174 of *Solid state ionics. 2004*. p. 271 - 277.

[29] Wiberg Nils. *Lehrbuch der Anorganischen Chemie*. Walter de Gruyter. 2007. 102 edition. p. 893 - 899.

[30] Shobit Omar. *Doped Ceria for Solid Oxide Fuel Cells*. IntechOpen. 2019. p. 43 - 53.

[31] Alexander K. Opitz, Markus Kubicek, Stefanie Huber, Tobias Huber, Gerald Holzlechner, Herbert Hutter, and Jürgen Fleig. *Thin film cathodes in SOFC research: How to identify oxygen reduction pathways?*, volume 28 of *Journal of Materials Research. 2013*. p. 2085 - 2105.

[32] Alexander K. Opitz, Alexander Lutz, Markus Kubicek, Frank Kubel, Herbert Hutter, and Jürgen Fleig. *Investigation of the oxygen exchange mechanism on Pt|Yttria stabilized zirconia at intermediate temperatures: Surface path versus bulk path*, volume 56 of *Electrochimica Acta. 2011*. p. 9727 - 9740.

[33] Cowin Peter, Petit Christophe, Lan Rong, Irvine John, and Shanwen Tao. *Recent progress in the development of anode materials for solid oxide fuel cells*. Advanced Energy Materials. 2011. 1 edition. p. 314-332.

[34] I. Riess. *Mixed ionic–electronic conductors—material properties and applications*, volume 157 of *Solid State Ionics. 2003*. p. 1 - 17.

[35] Dell R.M. and Rand D.A.J. *Energy storage - a key technology for global energy sustainability*, volume 100 of *Journal of Power Sources. 2001*. p. 2-17.

[36] Eason Robert. *Pulsed Laser Deposition of thin films, Applications - led growth of functional materials*. Wiley-Interscience. 2007. p. 3 - 11.

[37] Steinberger-Wilckens Robert. *Hochtemperaturbrennstoffzellen – Entwicklung neuer Materialien und Werkstoffe*. Forschungsverbund Sonnenerergie. 2004. p. 1 - 3.

[38] Srinivasan S. *Fuel cells: From fundamentals to applications*. Springer. 2006. p. 1 - 42.

[39] Wang Shaorong. *High temperature properties of $La_{0.6}Sr_{0.4}Co_{0.8}Fe_{0.2}O_{3-\delta}$ phase structure and electrical conductvity*, volume 159 of *Solid State Ionics. 2003*. p. 71 - 78.

[40] Badwal Sukhvinder, Munnings Christopher, and Kulkarni Aniruddha. *Review of progress in high temperature solid oxide fuel cells*, volume 50 of *ChemInform. 2014*. p. 23 - 37.

[41] Badwal Sukhvinder, Fini Daniel, and Munnings Christopher. *Structural and microstructural stability of ceria – gadolinia electrolyte exposed to reducing environments of high temperature fuel cells*, volume 36 of *Journal of Materials Cemistry A. 2013*. p. 10555 - 11080.

[42] R. J. D. Tilley. *Defects in solids*. Wiley and Sons. 2008. p. 1 - 10; 28 - 30.

[43] H Tuller. *Semiconduction and mixed ionic-electronic conduction in nonstoichiometric oxides: impact and control*, volume 94 of *Solid State Ionics. 1997*. p. 63-74.

[44] Rojek V.A. *Elektrochemische Charakterisierung von elektrolytgestützten Hochtemperaturbrennstoffzellen*. Freie Universität Berlin. 2013. p. 36 - 48.

[45] Chueh W. C., Hao Y., and Haile S.M. *High electrochemical activity of the oxide phase in model ceria–Pt and ceria–Ni composite anodes*, volume 11 of *Natural Materials. 2012*. p. 155 - 161.

[46] Jensen William. *Faraday's Laws or Faraday's Law?*, volume 89 of *Journal of Chemical Education. 2012*. p. 1208 - 1209.